University of Alberta

Development of an optical biosensor based on Mach-Zehnder Interferometry for detection of *Listeria monocytogenes*

by
Dibyo Sarkar

A thesis submitted to the Faculty of Graduate Studies and Research in partial fulfillment of the requirements for the degree of

Master of Science

Department of Mechanical Engineering

Fall 2013
Edmonton, Alberta

To My Mother

Abstract

Label-free optical biosensors are widely used for the detection of pathogens due to their low-cost, real-time detection and high sensitivity. A Mach-Zehnder Interferometer (MZI) based biosensor has been developed for the detection of gram-positive bacteria, Listeria monocytogenes. An extensive theoretical analysis of MZI configurations was performed to determine the critical dimensions for a high sensitivity monomodal waveguide. These MZI waveguides, with nanometer size ridge structure, were fabricated using standard micro/nanofabrication techniques. Using the fabricated MZI waveguides, an efficient optical immunoassay technique for the detection of Listeria was demonstrated. The MZI biosensor was able to detect Listeria at concentrations close to 10^5 cfu/ml, which is lower than the infection dose for human beings. SEM analysis and light intensity measurements showed the biosensor is highly selective to Listeria over other microbial species. Finally, a calibration scheme of the MZI biosensor was developed to determine an unknown concentration of Listeria in a given sample.

Acknowledgements

I would like to thank my supervisor, Dr. Sushanta K. Mitra, for his constant help and guidance in the last two years. He has been a wonderful mentor and I can happily admit that I have learnt a lot from him both professionally and personally. His patience and cooperation is what made the journey of my Masters program smooth and enjoyable. I am greatly indebted to him for his untiring efforts in improving my scientific writing skills. I am also very grateful to him for the amount of time he has spent in one-on-one discussions whenever I needed help with my research. It has been an honor to have known him and worked with him for the last two years.

I would also like to thank the members of my examining committee : Dr. Xihua Wang, Dr. Thomas Thundat and Dr. Marc Secanell Gallart, for reviewing my thesis.

I am grateful to all my fellow Micro and Nano-scale Transport Laboratory (MNTL) colleagues for their constant help and support. I would specially like to thank Dr. Siddhartha Das, Assistant Professor in the Mechanical Engineering department, University of Alberta, for his invaluable suggestions in the course of my research. He has always been a source of inspiration and a figure of respect to me. I would also like to extend my heartfelt gratitude to Naga Siva Kumar Gunda and Sheng Tian, for always taking time out from their busy schedule whenever I needed their help or advice. I would also like to thank Dr. Prashant R. Waghmare and Anil Stephen for their overwhelming support at numerous occasions.

I would like to acknowledge the financial supports from NSERC-CRD program and AQL Inc. It has been a pleasure working with Mr. Iqbal Jamal,

AQL Inc., and I am indebted to him for his valuable inputs during our monthly meetings. I am also grateful for the useful discussions with Stefania Dante, PhD student at Research Center on Nanoscience and Nanotechnology(CIN2), Spanish National Research Council (CSIC), Barcelona, Spain.

Most importantly, I want to take this opportunity to thank my parents for their unyielding faith in me. My mother has been my role-model since I was a child and it is because of her guidance and support that today I am pursuing my Masters at such an esteemed university.

I would also like to thank my B. Tech supervisor, Dr. Achintya K. Pramanick, for inspiring me to pursue Masters and for simply being the nicest person I have known. I am grateful to my friends Shankha Subhra Chatterjee, Ananya Gangopadhay, Santu Mandal, Neha Khanna and Chandan Kumar for helping me with cope up with the pressures of graduate studies and getting me through it. Finally, a heartfelt thanks goes to my girlfriend, Shaina Mahajan, who has been there for me at every step of this journey and most importantly for trying her best to show immense patience throughout.

Contents

List of Tables

List of Figures

Chapter 1

Introduction

1.1 Motivation

Microbes such as bacteria and viruses are found everywhere around us. From the food we eat and the water we drink to the air we breathe, we interact with various species of these microbes, although unknowingly, on a daily basis. A large number of these microbes are essential to nature and assist in the survival of human beings but there are certain species of micro-organisms which can be potentially harmful, often leading to serious infections and, in some cases, even death. *Listeria monocytogenes* is one such pathogen found in soil, vegetation (Weis and Seeliger, 1975), and water (Watkins and Sleath, 1981) that causes listeriosis, which can have a high mortality rate (Gellin and Broome, 1989) (25-30 %) in immune-compromised populations and pregnant women (Slutsker and Schuchat, 1999). *Listeria monocytogenes* was discovered in 1926 and the first human infection was reported three years later in the year 1929 in Nyfeldt, Denmark (Gray and Killinger, 1966). Since then, several sporadic outbreaks of human listeriosis (Baloga and Harlander, 1991; Bassler et al., 1995; Bille and Rocourt, 1996; Slutsker and Schuchat, 1999) have led to more focused research on the detection of this bacterium. *Listeria monocytogenes* can survive in harsh conditions and grow in temperatures ranging from -1.5^0C to -50^0C (Donnelly, 2001). This ability of *Listeria monocytogenes* to grow in refrigeration temperatures makes it a potent contaminant in ready-to-eat (RTE) food products (Schuchat et al., 1992; Schwartz et al., 1988). One

of the first identified cases of *L. monocytogenes* in food samples was in Nova Scotia, Canada (Schlech III et al., 1983) in 1981. Since then, numerous cases of food-borne listeriosis have cost millions of dollars to the Canadian food industry annually in terms of food re-calls. Commercially available detection techniques include enzyme-linked immunosorbent assay (ELISA), enzyme-linked immunofluorescence assay (ELFA), fluorescence in-situ hybridization (FISH), polymerase chain reaction (PCR), etc. (Bashir, 2004). However, the incubation periods involved in these techniques can range from several weeks to months, a time frame over which the contaminated RTE meat products would have left the processing plant and already been available to consumers in grocery stores. The main motivation for this work is to develop a biosensor with a small footprint that can quickly detect low-levels of *Listeria monocytogenes*. Such high sensitivity rapid detection methods would reduce the likelihood of contaminated RTE products, reduce costs associated with the storage of product at plants pending culture-based microbiological results, and increase shelf-life of products in the grocery stores.

1.2 Objective

Objective of the research presented here has been the development of label-free optical biosensors based on a Mach-Zehnder Interferometer (MZI) configuration for detection of *Listeria monocytogenes*. This involves, designing low-loss MZI waveguides to achieve high sensitivity biomolecule detection; developing a fabrication protocol using reproducible micro/nanofabrication techniques which can later facilitate mass production of the MZI biosensor chips; and validating the sensitivity and reliability of the detection technique by performing standard assay tests.

1.3 Structure of the Thesis

The guidelines from the Faculty of Graduate Studies and Research (FGSR)at the University of Alberta have been followed to prepare the thesis and this

thesis is arranged into the following four chapters:

This first chapter presents the motivation and the problem statement of this research.

Chapter 2 provides a detailed theoretical study of light wave equations for designing an efficient monomodal waveguide with an integrated Mach-Zehnder Interferometer (MZI) configuration. Simulation studies; fabrication procedures; and experimental results, validating the simulation studies, have also been described in this chapter.

Chapter 3 demonstrates an efficient optical immunoassay technique for the detection of *Listeria monocytogenes* using the MZI waveguides described in Chapter 2. The MZI biosensor was able to detect *L. monocytogenes* at concentrations of the order of $10^5 cfu/ml$, which is lower than the infection dose for human beings. SEM analysis and light intensity measurements showed the biosensor is highly selective to *L. monocytogenes* over other microbial species (such as *Escherichia coli*).

Finally Chapter 4 summarizes the key findings of this research. Future work based on the outcome of this research have also been recommended.

References

A. Baloga and S. Harlander. Comparison of methods for discrimination between strains of listeria monocytogenes from epidemiological surveys. *Applied and environmental microbiology*, 57(8):2324–2331, 1991.

R. Bashir. Biomems: state-of-the-art in detection, opportunities and prospects. *Advanced drug delivery reviews*, 56(11):1565–1586, 2004.

H. A. Bassler, S. J. Flood, K. J. Livak, J. Marmaro, R. Knorr, and C. A. Batt. Use of a fluorogenic probe in a pcr-based assay for the detection of listeria monocytogenes. *Applied and environmental microbiology*, 61(10):3724–3728, 1995.

J. Bille and J. Rocourt. Who international multicenter *Listeria monocytogenes* subtyping studyrationale and set-up of the study. *International journal of food microbiology*, 32(3):251–262, 1996.

C. W. Donnelly. Listeria monocytogenes: a continuing challenge. *Nutrition reviews*, 59(6):183–194, 2001.

B. Gellin and C. Broome. Listeriosis. *Journal of the American Medical Association*, 261(9):1313–1320, 1989.

M. L. Gray and A. Killinger. Listeria monocytogenes and listeric infections. *Bacteriological Reviews*, 30(2):309, 1966.

W. F. Schlech III, P. M. Lavigne, R. A. Bortolussi, A. C. Allen, and E. V. Haldane. Epidemic listeriosis: evidence for transmission by food [listeria monocytogenes]. *New England journal of medicine*, 308, 1983.

A. Schuchat, K. A. Deaver, J. D. Wenger, B. D. Plikaytis, L. Mascola, R. W. Pinner, A. L. Reingold, C. V. Broome, B. Swaminathan, P. S. Hayes, et al. Role of foods in sporadic listeriosis. *JAMA: the journal of the American Medical Association*, 267(15):2041–2045, 1992.

B. Schwartz, C. Broome, G. Brown, A. Hightower, C. Ciesielski, S. Gaventa, B. Gellin, L. Mascola, et al. Association of sporadic listeriosis with consumption of uncooked hot dogs and undercooked chicken. *The Lancet*, 332 (8614):779–782, 1988.

L. Slutsker and A. Schuchat. Listeriosis in humans. *Food Science and Technology*, pages 75–96, 1999.

J. Watkins and P. K. Sleath. Isolation and enumeration of Listeria monocytogenes from sewage, sewage sludge and river water *Journal of Applied Microbiology*, 50(1):1–9, 1981

J. Weis and H. P. Seeliger. Incidence of Listeria monocytogenes in nature *Applied Microbiology*, 30(1):29–32, 1975

Chapter 2

Analysis, Design and Fabrication of optical waveguides for Mach-Zehnder Interferometry [1]

2.1 Introduction

Optical waveguides are used in large number of science and engineering areas with wide range of applications - from detection of biomolecules to homeland security. Typically, optical waveguides consist of a middle core layer and two outer cladding layers. The core layer has a higher refractive index than the cladding layers which allows light to propagate through the core due to total internal reflections. There has been a sudden surge in research towards design and fabrication of such optical waveguides (Chou and Krauss, 1997; Bruck et al., 2011; Crunteanu et al., 2002; Rickman et al., 1994; Soref and Larenzo, 1986). However, still certain challenges exists in terms of obtaining desired "quality" of the waveguide. In this paper, we provide a systematic approach towards the design and fabrication of waveguides, typically for MEMS (Micro-ElectroMechanicalSystem) applications.

Often, in MEMS applications, a ridge structure is fabricated in the core layer to confine the light waves and guide them through the waveguide (Syms and

[1] A version of this chapter has been published in *Optics Communications*, Vol. 311, pp. 338-345, 2013.

Cozens, 1992). Due to the difference in the refractive indices of core and cladding layers, these layers will have different wave equations. Hence, there would be a discontinuity in the electromagnetic field at the core-cladding interface. This discontinuity is compensated by an exponentially decaying electromagnetic field at the core-cladding interface called the evanescent field. The evanescent field has a penetration depth of 100-200 nm (Rohrbach, 2000) for a 632.8 nm wavelength light emitted from a He-Ne laser. In number of MEMS applications, this evanescent field of the waveguide is often manipulated to act as a sensing mechanism for detection of biomolecules (Brosinger et al., 1997; Lechuga et al., 2009; Prieto et al., 2003; Parriaux and Veldhuis, 1998).

Figure 2.1 shows a Mach-Zehnder Interferometer (MZI) configuration waveguide, based on the principle of total internal reflection (TIR), on a silicon substrate. Existing literature suggests that there are different interferometer configurations available for 3-dB coupling such as Multimode Interferometers (MMI) (Soldano and Pennings, 1995; Spiekman et al., 1994; Themistos and Rahman, 2002); Directional Couplers (DC) (Forber and Marom, 1986; Wen, 1970). These interferometers have some inherent challenges and limitations which include lack of single mode light field in MMIs (lower sensitivity) and complexity of fabrication of DCs. In this present study, we have focussed on an MZI configuration waveguide with Y-junction 3-dB couplers which has shown to overcome these challenges (Frandsen et al., 2004; Izutsu et al., 1982; Liu et al., 2008). The design consists of two Y-junction couplers connecting a sensor and a reference arm. A portion of the sensor arm has its upper cladding layer etched out exposing the core layer called the sensing area. All the biofunctionalization takes place at the sensing area allowing for the effect of the evanescent field to come into play at the core boundary. Incoming light is split into the two arms which later recombine providing output signal containing information of the changes that have occurred in the sensor arm. The sensor arm is the site where the refractive index change takes place. This causes a phase shift in the sensor arm as compared to the reference arm. As mentioned earlier, the distortion in the evanescent field for the sensing arm with respect

to the reference arm is captured by a photodiode (Lechuga et al., 2009; Prieto et al., 2003; Parriaux and Veldhuis, 1998).

This work, for the first time, advances the quantitative basis for the design of Si-based Mach-Zehnder Interferometers meant for optimal biomolecule detection. MZI based biosensors have seen huge changes in their design since their advent in 1993 by Heideman et al. (Heideman et al., 1993). Although polymers such as PMMA (polymethylmethacrylate), polyamide, polysterene, etc. had been used to fabricate waveguides since the 1970s (Harris et al., 1970) and more recently have been used in MZI-based biosensing (Bruck and Hainberger, 2008; Bruck et al., 2011; Esinenco et al., 2005; Műller et al., 2005), silicon based waveguides have always been the preferred choice due to their much higher sensitivity (Heideman et al., 1993; Prieto et al., 2003). As already discussed, in MZIs, Y-junction couplers are more advantageous than MMIs or DCs and this has ensured that most of the recent studies on MZI-based biosensors have frequently used Y-junctions with circular bends of radius $80mm$ (Lechuga et al., 2009; Prieto et al., 2003; Sepulveda et al., 2006; Zinoviev et al., 2008). However, there is little discussion on the design of the Y-junctions used on these MZI configurations. Therefore, a very relevant question pertains to quantifying the physical dimensions of Y-junction MZIs based on silicon technology. But to the authors' best knowledge, there is no literature on theoretical analysis and design of Si-based MZI. Our study bridges this crucial gap by providing an explanation through theory and simulations as to why such dimensions have been used over the years and where the cut-off dimension of the Y-junction lies.

Optical waveguides (or fibers) can be classified into two broad categories: monomode and multimode. Monomode optical fiber allows only the lowest order bound mode (or the zeroth mode) to propagate whereas a multimode fiber, as the name suggests, allows higher modes to propagate through it. The use of monomode waveguides for optical biosensing, in order to achieve high sensitivity, has been known in literature for over two decades (Lechuga et al., 2009; Lukosz, 1991; Nellen and Lukosz, 1993; Nellen et al., 1988; Prieto et al.,

2003; Sloper et al., 1990). Therefore, in order to achieve a high sensitivity immunosensor that can detect biomolecule concentration levels lower than 100 CFU/ml, it is imperative to design an optical waveguide capable of rejecting any mode other than the fundamental mode from propagating through it.
In this paper, we have performed simulations on various planar waveguide dimensions to establish that monomode waveguides indeed provide the highest sensitivity. Detailed theoretical analysis of the waveguides have also been presented. Through our simulations we have obtained optimal dimensions for a Mach-Zehnder Interferometer (MZI) configuration with the highest sensitivity in the form of lowest optical losses during light propagation. Such simulation results present to us a range of waveguide dimensions that can be used for monomode propagation. We selected an optimal dimension among those simulated waveguides for further microfabrication process. Also, from the existing literature it is observed that obtaining such precise sub-micron feature waveguide (as required for monomode waveguides), yet having all necessary properties related to the core and cladding materials, is of great challenge. Although there are quite a few novel fabrication technologies for fabricating sub-micron features, for example, the work done by Chou et al. (Chou and Krauss, 1997) and others (Bruck et al., 2011; Crunteanu et al., 2002; Rickman et al., 1994; Soref and Larenzo, 1986), yet they are accompanied by complexities while fabricating features with dimensions as low as 4nm. Our main motivation was to use cheap and reproducible fabrication techniques which overcome challenges typically associated with fabrication of such waveguides and obtain the desired feature sizes, as inferred from our simulation study.

2.2 Principles and simulations

2.2.1 Design considerations

The design for the waveguide is based on the principle of monomodal propagation of light. To ensure that there is monomodal propagation of light as opposed to multimodal propagation in order to nullify the effect of Intermodal

Dispersion (or Differential Mode Delay), the waveguide should have specific dimensions. The core and cladding dimensions are already well established in literature (Heideman and Lambeck, 1999; Pal, 1992). For example, for a waveguide to be monomodal, one can define a characteristic quantity, V, given as (Marcuse, 1976):

$$V = \frac{2\pi a}{\lambda}(n_{Co}^2 - n_{Cl}^2)^{1/2} \tag{2.1}$$

where, a is the core half width, n_{Co} and n_{Cl} are the refractive indices of the core (silicon nitride) and cladding (silicon dioxide), respectively and λ is the wavelength of the source. The V number is typically less than 2.405 for a monomodal waveguide. Equation 2.1 shows that for the V number to be less than 2.405, the half width (a) should be less than 177nm, which means that the total width of the core can be of maximum dimension of 354nm. However, the sensing area of the biosensor would have the upper cladding layer etched out and replaced with a layer of biomolecules (bacteria), which have a lower index of refraction (Balaev et al., 2003; Jonasz et al., 1997). This constrains the core width even further and hence a safe design would have a 250nm wide core.

The ridge plays the most important role in deciding the modal behavior of a waveguide. Finding out the dimensions of the ridge is non-trivial and involves computing mode profiles and solving wave equations. This has been done through simulations using RSOFT CAD^{TM}, a photonic design software, by RSoft Design Group, Inc. Another key design aspect is the Y-junction of MZI system. An MZI configuration essentially has two Y-junctions, one that diverges the input to the sensor and reference arms while the other converges the sensor and reference arms to the output. The highest amount of losses in such a configuration occurs due to bending losses in the Y-junctions. Therefore the Y-junctions need to be designed such that there is minimal bending loss without allowing cross coupling of signal between the sensor and reference arms.

2.2.2 Numerical Analysis

Figure 2.2 is a graphic representation, generated by RSOFT CAD^{TM}, of the boundary conditions used for the simulations. The 1.5μm lower cladding layer and 1.75μm upper cladding layer have a refractive index of 1.46, representing the SiO_2 cladding layers. The 250 nm core layer, with a refractive index of 2.00, represents the Si_3N_4 core layer and has a 4μm by 4nm ridge. The total length of the chip in the z-direction (not shown in figure) is 30mm.
RSOFT CAD^{TM} uses a Finite Difference Beam Propagation (FDBP) method to solve exact and paraxial wave equations derived from the Helmholtz equation (Scarmozzino et al., 2000). The computational effort is directly proportional to the number of grid points used in the numerical simulation.
Light propagation within the waveguide can be described in terms of the Helmholtz equation as (Moar et al., 1999):

$$\nabla^2\Phi(r) + k^2n^2\Phi(r) = 0 \tag{2.2}$$

where, Φ is the electric field potential, $r = r(x, y, z)\epsilon R^3$, $k(= 2\pi/\lambda)$ is the free space wave number and $n(= n(x, y, z))$ is the refractive index of the device.
The electric field potential (Φ) in Eq. 2.2 gives the spatial dependence of the electric field E. The time dependence of the electric field can be re-written in terms of the field potential through the exponential term, as shown here (Syms and Cozens, 1992),

$$E(x, y, z, t) = \Phi(x, y, z)e^{i\omega t} \tag{2.3}$$

In a typical waveguide, the electric field potential varies rapidly in the z-direction (direction of propagation of the field). We factor out this rapid variance by substituting with a slowly varying field ψ, which can be written as (Snyder and Love, 1983):

$$\Phi(x, y, z) = \psi(x, y, z)e^{in_{Cl}kz} \tag{2.4}$$

where, n_{Cl} is a reference refractive index or, in this case, the cladding refractive index (refer Fig. 2.2).

The Helmholtz equation, provided in Eq. 2.2 can be expanded as,

$$\frac{\partial^2\Phi}{\partial x^2}+\frac{\partial^2\Phi}{\partial y^2}+\frac{\partial^2\Phi}{\partial z^2}+k^2n^2\Phi=0 \tag{2.5}$$

Now replacing Eq. 2.4 in Eq. 2.5, we get

$$\frac{\partial^2\psi}{\partial x^2}+\frac{\partial^2\psi}{\partial y^2}+\frac{\partial^2\psi}{\partial z^2}+2in_{Cl}k\frac{\partial\psi}{\partial z}+\psi(n^2-n_{Cl}^2)k^2=0 \tag{2.6}$$

which is often referred as the *exact wave equation*.

Based on the paraxial approximation that ψ varies very slowly with z, one can write (Feit et al., 1979):

$$\frac{\partial^2\psi}{\partial z^2}\ll\frac{\partial\psi}{\partial z} \tag{2.7}$$

which gives rise to a *Parabolic* or *Fresnel* form of the wave equation:

$$\frac{\partial^2\psi'}{\partial x^2}+\frac{\partial^2\psi'}{\partial y^2}+2in_{Cl}k\frac{\partial\psi'}{\partial z}+\psi'(n^2-n_{Cl}^2)k^2=0 \tag{2.8}$$

Since the waveguide is translationally invariant, i.e., the refractive index does not vary in the z-direction ($n=n(x,y)$), the input for this analysis is mainly the index distribution in the x and y directions (see Fig. 2.2). The wavelength of the light at the input (z=0) is also provided and the FDBP numerical analysis computes the wave field throughout the domain ($0\leq z\leq 30mm$).

The next part of the simulations is to calculate the number of modes in the waveguide. As the waveguide needs to be a monomode waveguide, modal analysis is a critical part of the whole design. In order to do this, a propagating beam method is used (Feit et al., 1980). This technique generates correlation functions by solving the wave equations to compute the modes in a structure. The general solutions to Eqs. 2.6 and 2.8 can be expressed as eigenfunction expansions,

$$\psi(x,y,z)=\sum_n A_n u_n(x,y)e^{-i\beta_n z} \tag{2.9}$$

$$\psi'(x,y,z)=\sum_n A'_n u'_n(x,y)e^{-i\beta'_n z} \tag{2.10}$$

where u is the eigenfunction and A is a constant. Here, β is the propagation constant, which describes the behavior of a mode in the waveguide. The relation between β_n and β'_n is given as (Feit et al., 1980),

$$\beta_n=-n_{Cl}k[1-(1+2\beta'_n/n_{Cl}k)^{1/2}] \tag{2.11}$$

Therefore, once the simpler Fresnel (parabolic) equation (Eq. 2.10) is solved and β'_n is calculated, it is easy to find the propagation constant (β_n) for the exact wave equation or the Helmholtz equation.

RSoft uses a correlation function that relates the contribution of the field at $z = 0$ over the whole range of the function (parabolic). The correlation function (C) is represented as,

$$C(z) = \int\int \psi'(x, y, 0)\psi'(x, y, z)dxdy \tag{2.12}$$

For different modes ($j = 0, 1, 2...$), one can write:

$$\psi'(x, y, z) = \sum_{n,j} A'_{n,j} u'_{n,j}(x, y)e^{-i\beta'_n z} \tag{2.13}$$

Substituting Eq. 2.13 in Eq. 2.12, one obtains:

$$C(z) = \sum_{n,j} |A'_{n,j}|^2 e^{-i\beta'_n z} \tag{2.14}$$

A Fourier transform of the correlation function is performed with respect to the axial z-direction. The resulting spectra display sharp resonances corresponding to mode groups, and the positions and heights of these resonances determine the mode properties (β). The Fourier transform of Eq. 2.14 is,

$$C(\beta) = \sum_{n,j} |A'_{n,j}|^2 \int_{-\infty}^{\infty} e^{i(\beta-\beta'_n)z} dz \tag{2.15}$$

By introducing a Delta function (Olver et al., 2010),

$$\delta(\beta - \beta'_n) = \int_{-\infty}^{\infty} e^{i(\beta-\beta'_n)z} dz \tag{2.16}$$

one can re-write Eq. 2.15 as (Feit et al., 1980),

$$C(\beta) = \sum_{n,j} |A'_{n,j}|^2 \delta(\beta - \beta'_n) \tag{2.17}$$

Since $\delta(0)$=1, Eq. 2.17 will give a spectra where the maxima is at $\beta = \beta'_n$. This gives the β'_n values which in turn lead to β_n values from Eq. 2.11. These values are used to find the field profiles by placing them in the eigenfunctions (Eqs 2.9 and 2.10).

2.2.3 Results of simulation

The propagation constant β provides information related to the amount of losses in each mode. Since, the main focus is on developing low loss fundamental mode waveguides, different combinations of width (w) and height (h) (refer to Fig. 2.1) of the ridges are tried out to find an optimal design. It is found that waveguides with ridge width below 8μm and height between 1 to 4nm showed monomodal behavior. Table 2.1 enlists different combinations of the ridge width(w) and height(h) with the modulus of the propagation losses (calculated from β) occurring in each of them. Based on the calculated values

Table 2.1: Propagation losses in the fundamental mode or zeroth order mode (the only mode of light propagating in a monomode waveguide) for different combinations of ridge dimensions.

w \ h	1nm	3nm	4nm
2μm	1.185x10^{-7}	2.769x10^{-9}	1.353x10^{-9}
3μm	4.93x10^{-8}	9.401x10^{-10}	1.125x10^{-10}
4μm	2.496x10^{-8}	3.87x10^{-10}	**1.373x10^{-10}**
5μm	1.315x10^{-8}	8.977x10^{-11}	3.12x10^{-10}
6μm	6.518x10^{-9}	9.585x10^{-11}	2.487x10^{-10}
7μm	2.849x10^{-9}	2.995x10^{-10}	bimode

of monomode losses within the waveguide, the dimensions chosen for fabricating the waveguides are $h = 4nm$ and $w = 4\mu m$, which provides one of the minimal losses, as highlighted in Table 2.1.

The next step is to design the MZI structures. We perform simulations on two different geometries. One of them has straight arms with an opening angle θ called the *angular Y-junction* while the other one has an S-bend of radius R called the *Sbend Y-junction* (see Fig. 2.3). All simulations were done with the distance between the two arms (d) not exceeding $100\mu m$, since the arms need to be close to each other to ensure that there is no phase change signal at the output due to the difference in variations of temperature, humidity, etc. in the two arms (Lechuga et al., 2009). Simulation results show that for a

constant value of the arm length L, the Sbend configuration shows less loss than an angular configuration. For example, for $L = 22mm$, the loss incurred in Sbend is $0.4dB/cm$ whereas for angular it is $0.56dB/cm$. On repeating such simulations for various dimensions, it is found that the best results were seen for angular bends with $\theta < 2.5°$ and Sbends with $R > 15mm$. Figure 2.4 compares angular bend structure with different θ values (1° and 3.37°). The one with an angle higher than 2.5° is observed to have large loss (nearly $3dB/cm$) and the presence of a higher order mode in the vertical arms. This can be explained by a phenomenon called intermodal scattering. Sharp bends in the MZI design cause intermodal scattering, where a fraction of power from the fundamental mode is transferred to a higher order mode (Syms and Cozens, 1992). The appearance of a higher order mode in the waveguide just after the diverging (or input) Y-junction can explain why the loss distribution is not symmetric (refer to Fig. 2.4(ii)(b)). Higher order modes are much more susceptible to bend losses as compared to the fundamental mode and therefore the losses are much higher in the waveguide section just after the output Y-junction than in the region just before the input Y-junction.

Decreasing θ to a much lower value and increasing R to a much higher value is constrained by the size of the chip. One possible solution is to decrease d and bring the arms closer. However, the two MZI arms cannot be brought closer than $70\mu m$ as cross coupling of signal between the two arms can occur.

2.3 Materials and dimensions

For the fabrication of the optical waveguides, silicon nitride (R.I. = 2.00) is chosen as the core material while silicon dioxide (R.I. = 1.46) forms the cladding layers. Silicon nitride was selected as the core of the waveguide because it is chemically stable and does not allow liquids to diffuse into it from outside during biofunctionalization steps, which are often used in biosensor application (Heideman and Lambeck, 1999). With silicon nitride as the core, silicon dioxide was selected as the upper and lower cladding layers since it is

a well established fact that a large difference in core and cladding refractive indices has a direct effect on improving sensitivity of the waveguide (Lukosz, 1991; Tiefenthaler and Lukosz, 1989). Moreover, since both silicon nitride and silicon dioxide are transparent, light propagates through the waveguide without significant attenuation (Jones, 2010). The cross sectional view of the waveguide is shown in Fig. 2.5. Ideally the core layer should have a height of 250 nm and the upper and lower cladding layers should be more than 1.5 μm so that the cladding layer is sufficiently thicker than the core thickness in order to have low attenuation losses (Heideman and Lambeck, 1999; Pal, 1992). Based on the simulation results, *angular* Y-junctions with θ ranging from 0.9° to 2.5° and *S-bend* Y-junctions with R ranging from $20mm$ to $180mm$, can be the ideal dimensions for MZI system. However, in all of the designs the ridge height and width was fixed at 4nm and $4\mu m$, respectively. The length of the waveguide is typically about $30mm$.

2.4 Fabrication

We fabricated waveguides with MZI structures of $4nm$ height and $4\mu m$ width. Such low aspect ratio features possess inherent complications in fabrication. The fabrication involved nine major steps and all of the fabrication steps were performed in the NanoFab facility and the Micro and Nano-scale Transport Laboratory at the University of Alberta.

First, the Si wafers are cleaned in a piranha solution with 3 parts H_2SO_4 and 1 part H_2O_2, for 15 minutes. Then in order to obtain a high quality oxide layer with high uniformity to form the lower cladding, thermal oxidation is preferred since it is very important to have maximum uniformity before deposition of the core Si_3N_4 layer. Low Pressure Chemical Vapor Deposition (LPCVD) of Si_3N_4 is performed on the thermally oxidized Si wafer. LPCVD nitride can easily be deposited in a very pure and uniform way which leads to high thermal stability and low etch rates (Williams et al., 2003). Low etch rate is an essential advantage of LPCVD because it can allow etching of features with depths as small as 4 nm. Then, in the most important step of

the fabrication procedure, photolithography and Reactive Ion Etching (RIE) are used to print the MZI configuration on the Si_3N_4 core. The mask used for the photolithographic step was designed using a mask generation software from Tanner EDA, L-Edit. The SiO_2 upper cladding layer does not demand too much of uniformity but it is very essential that the stress induced by the deposition of a thick upper cladding layer is well controlled. Hence Plasma Enhanced Chemical Vapor Deposition (PECVD) process was used for forming the upper cladding layer.

Till this point, a complete MZI waveguide with two reference arms has been fabricated. In order to create a sensing area on one of the arms (to be called as the sensor arm), another photolithographic and RIE step is performed. In this case, the SiO_2 upper cladding layer is selectively etched up to the core layer over a 20mm by 100μm area, thereby exposing the core-cladding boundary where the intensity of the evanescent field is the strongest (refer Fig.2.1). Once the chips were fabricated, the end faces were polished using diamond lapping and polishing films ($15\mu m$ to $0.1\mu m$). This step was essential to prevent scattering of light at the input and output of the waveguide.

Figure 2.6(b) is the microscopic image of a diverging Y-junction of one of the MZI structures with an *angular* Y-junction of one degree. Figure 2.6(c) is the microscopic image of the area on one of the MZI arms where the upper silicon dioxide cladding layer is completely etched to reveal the silicon nitride core layer (also called the sensor area).

2.5 Results

2.5.1 Thickness of layers and refractive indices

Ellipsometry is used for determining the thickness and more importantly the refractive indices of the SiO_2 cladding layers and the Si_3N_4 core layer. This system measures the thickness optically and hence is a non-destructive technique. The thermally grown SiO_2 layer (refer to section 2.4) is measured using an ellipsometer and it revealed a thickness of 1.3525 $\pm$ 0.0007 μm. The re-

fractive index was found to be 1.4668 ± 0.0012 which is close to the target refractive index of 1.46. The LPCVD nitride (refer to section 2.4) thickness was 252.6 ± 0.3 nm with a refractive index of 2.0844 ± 0.0051 which is again close to the target refractive index of 2. The upper cladding layer was found to be 1.9964 ± 0.0030 μm thick with a refractive index of 1.4631 ± 0.0012. All measurements were taken in the spectral range of 0.3μm to 0.8μm.

2.5.2 AFM

The ridge dimensions are measured using Atomic Force Microscopy (AFM). These AFM measurements are done after the first RIE step. Figure 2.7 shows 2-D and 3-D images of a 50 x 50μm area on the MZI chip where the diverging Y-junction is located. The RMS roughness was also calculated over various sections of the chip before and after PECVD of the SiO_2 upper cladding layer and it was found to be in the range of 0.5-0.6nm, which is acceptable.

2.6 Experimental setup

Figure 2.8 is a picture of the experimental setup used for analyzing the fabricated MZI chips. Light from a He-Ne laser ($633nm$) is coupled onto the MZI chip using a 40x objective lens. Light emitted by the chip is directly coupled into a multimode fiber ($62.6\mu m$ core diameter). The multimode fiber transmits the light into a photodiode for power measurements. The chip is placed on an XYZ stage with a piezo controlled resolution of $20nm$. In order to align the laser light into the sub-wavelength core ($250nm$), a CMOS camera, connected to a PC, is placed above the chip to simplify the optical alignment of the device.

In order to analyze the fabricated waveguides, loss measurements are conducted for the MZI chips. The loss per unit length can be written as (Grote and Venghaus, 2001):

$$dB/cm = \frac{10\log(P_{in}/P_{out})}{L} \tag{2.18}$$

where, P_{in} and P_{out} are the input and output powers of the waveguide, respectively, and L is the length of the whole chip ($30mm$).

Initially, the power at the input end of the waveguide (or the output from the laser), P_{in}, was compared to the power emanated by the waveguide, P_{out}. It is to be noted that, during experiments, the output from the laser is in the order of milliwatts(mW) whereas the output from the waveguide is in microwatts(μW). This indicates that a fair amount of light from the laser failed to enter the waveguide thereby creating anomalies in the loss analysis. Therefore, instead of measuring P_{in} as the power from the laser, the waveguide is cut into half and the corresponding output power from the chip of length $L/2$ is taken to be P_{in} while P_{out} remained the output power from an entire chip. Using this in Eq. 2.18 and making the length half of its original value ($L = 15mm$), the actual loss per cm of the waveguide was determined. Figure 2.9 (a) and (b) show the image of monomodal light field at the output end of the entire chip and at the section cut across the mid-way between the input and the output Y-junctions, respectively. The two spots in such mid-section (Fig. 2.9(b)) are due to light emitting from the two arms (reference and sensing) of the fabricated MZI.

The losses calculated range from $0.1dB/cm$ to $0.7dB/cm$ which follow the simulation results very closely. A comparison of the loss values calculated through simulations and experiments for different MZI configurations is given in Fig. 2.10. Propagation loss (dB/cm) values are plotted against increasing R values for Sbend (Fig. 2.10(a)) and θ values for angular (Fig. 2.10(b)) MZI configurations. The chips used for loss measurements do not have a sensing area etched on them. During biosensing experiments, the etched sensor area would encounter losses due to the discontinuity in the upper cladding. However, as biomolecules start immobilizing on the sensor surface, it is expected that the losses would start to decrease with an increase in concentration of the in situ biomolecule solution.

2.7 Conclusions

In this study, we have performed simulations for determining waveguide dimensions for monomodal propagation of light using RSOFT CAD^{TM}. Extensive theoretical analysis for mode calculation in waveguides has been shown. Two aspects of the design of MZI waveguides are taken into consideration. First, a monomodal waveguide was designed. Numerical solutions of the theoretical wave equations gave mode profiles of different waveguide configurations. A $4nm$ high and $4\mu m$ wide ridge structure was chosen as the dimension for fabrication. Second, the MZI configuration is designed. The choice of waveguide configurations have been done through loss analysis. For the first time, a dimensional constraint of the MZI configuration has been quantified for optical biosensors. From our simulation results, we have inferred that waveguides with Y-junctions above a 2.5° angle or below a $15mm$ radius will have extremely high losses. The fabrication steps involved in making sub-micron optical MZI waveguides have also been discussed. Finally, we performed loss analysis experiments on the fabricated MZI chips to confirm our simulation results and found them to be in congruence with each other. The characterization of fabricated waveguide through measuring the loss component further confirmed that the fabricated waveguide can be used for biosensors and other MEMS applications.

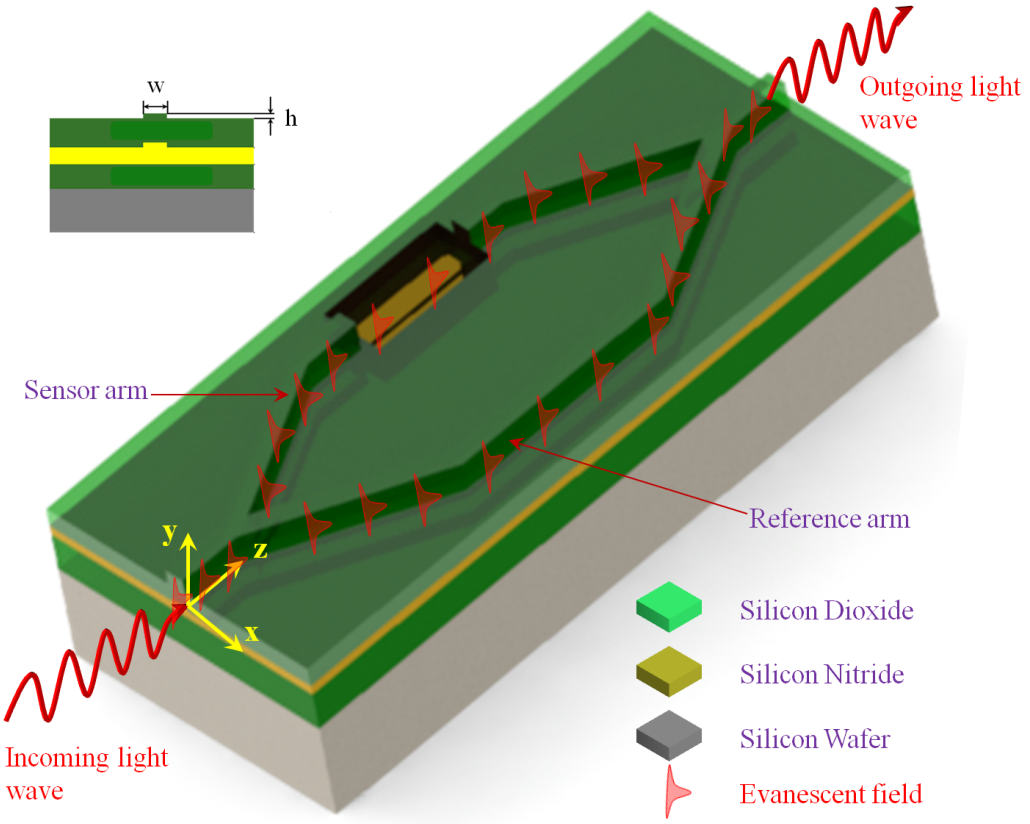

Figure 2.1: Schematic of a biosensor using Mach-Zehnder Interferometer configuration.

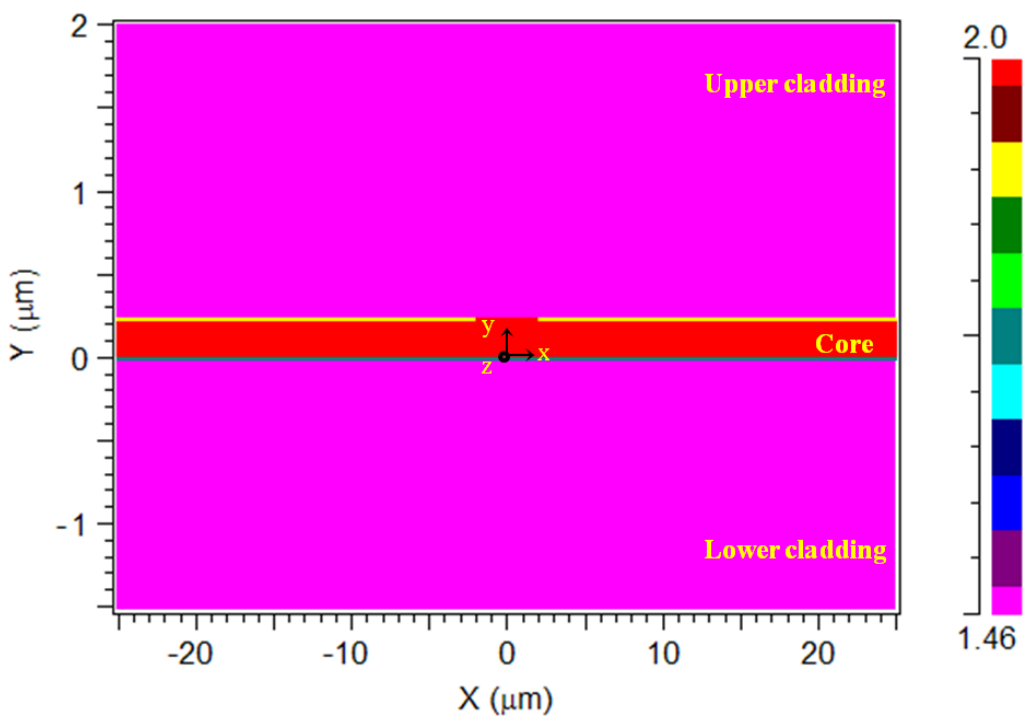

Figure 2.2: Cross-sectional refractive index layout of the waveguide at z=0. The z-axis is into the plane of the paper. The color bar to the right indicates the change in refractive index of the waveguide.

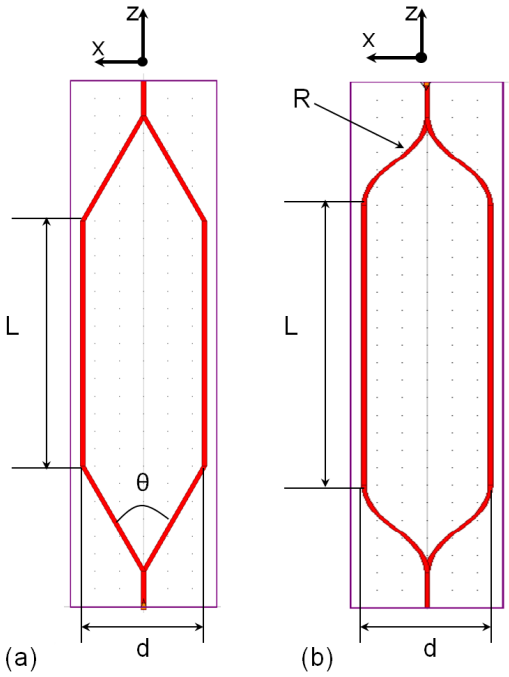

Figure 2.3: (a) Angular Y-junction, (b) Sbend Y-junction.

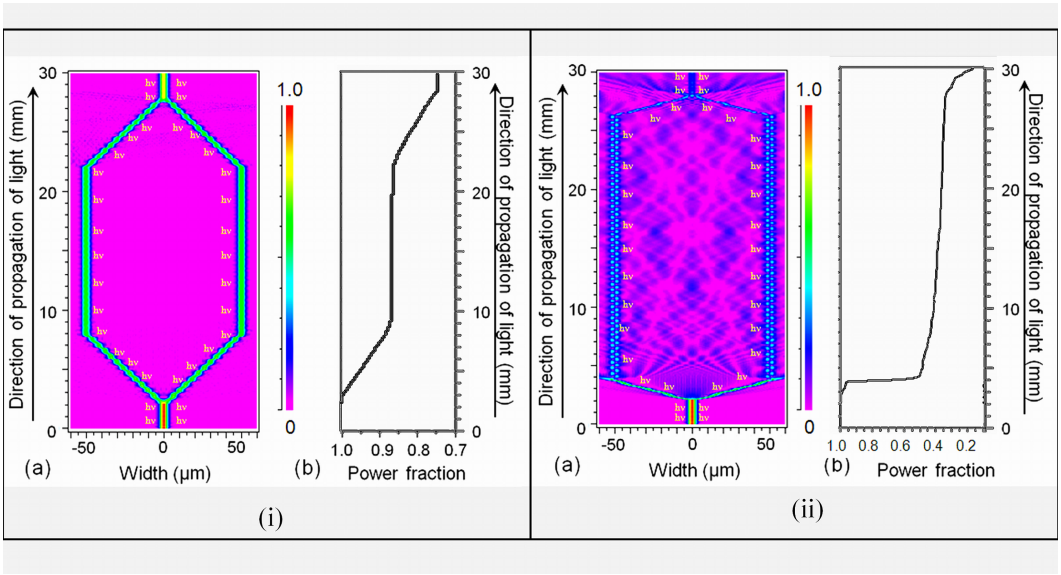

Figure 2.4: (i) a) Transverse electric field through the entire length of the MZI configuration ($\theta = 1°$), (b) Variation of power with length; (ii) a) Transverse electric field through the entire length of the MZI configuration ($\theta = 3.37°$), (b) Variation of power with length.

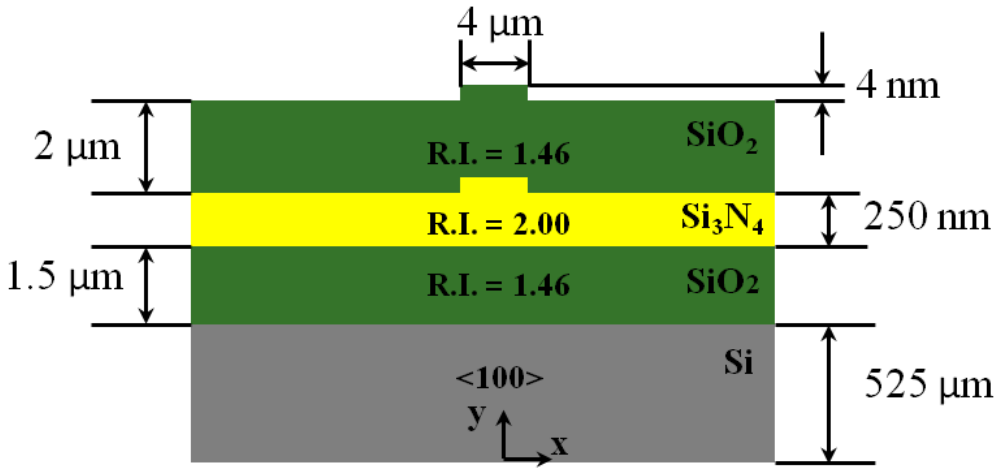

Figure 2.5: Cross sectional view of the waveguide with dimensions.

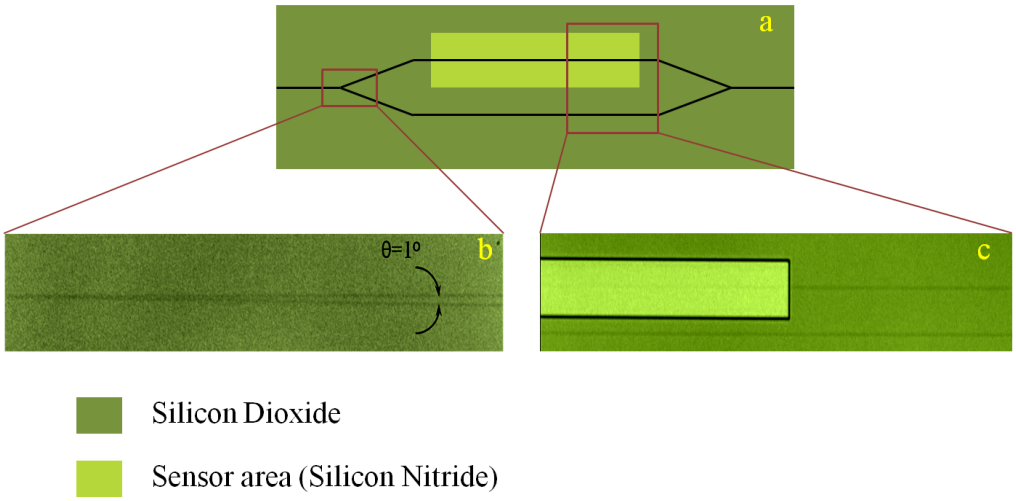

Figure 2.6: (a) Schematic of an MZI configuration, (b) Microscopic image of the diverging Y-junction (showing θ=1°), (c) Microscopic image of a portion of the sensor area revealing the silicon nitride core layer.

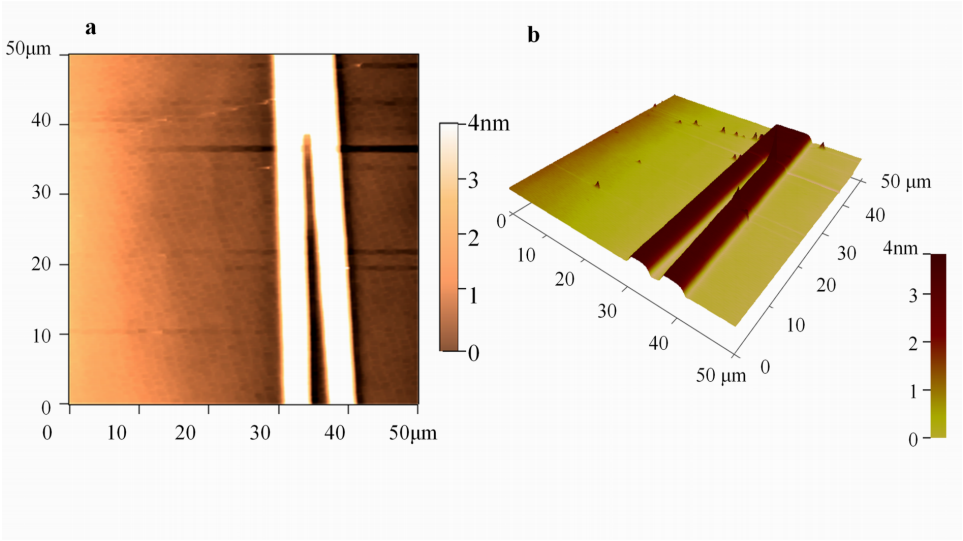

Figure 2.7: (a) 2-D AFM image of a diverging Y-junction scanned over an area of 50 x 50 μm on the MZI chip, (b) 3-D image of the Y-junction.

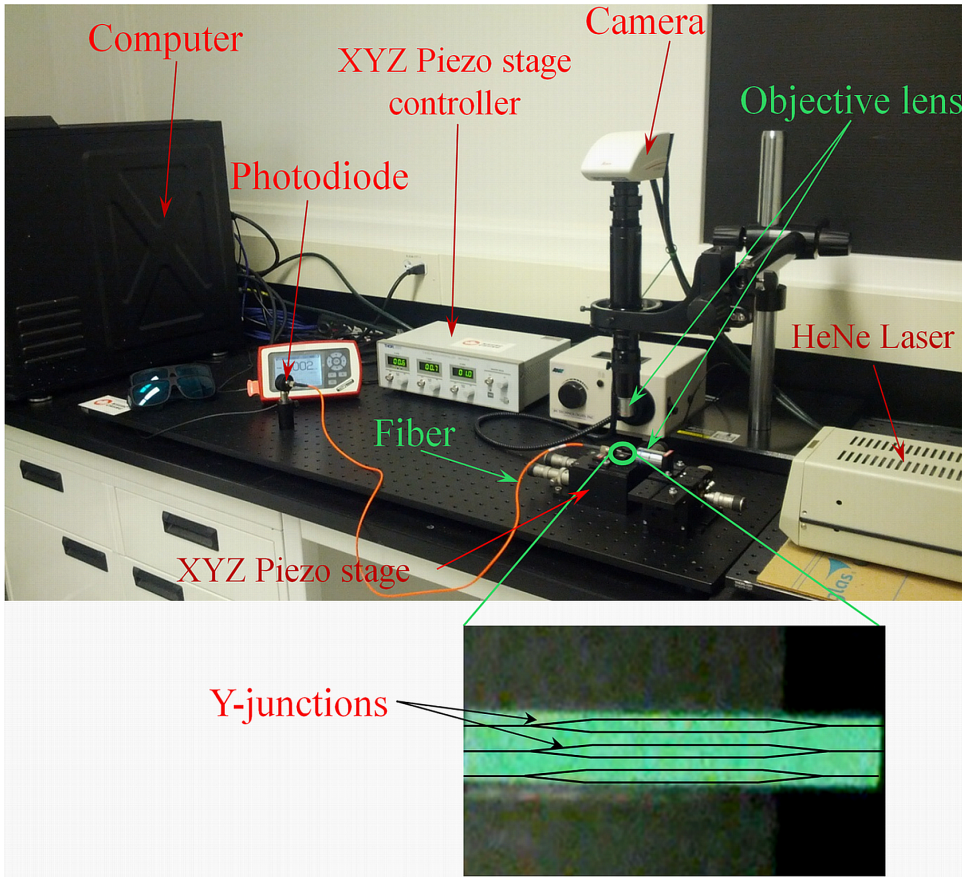

Figure 2.8: Laboratory setup of our experiment used for power measurements of the intensity of the light emanating from the waveguide.

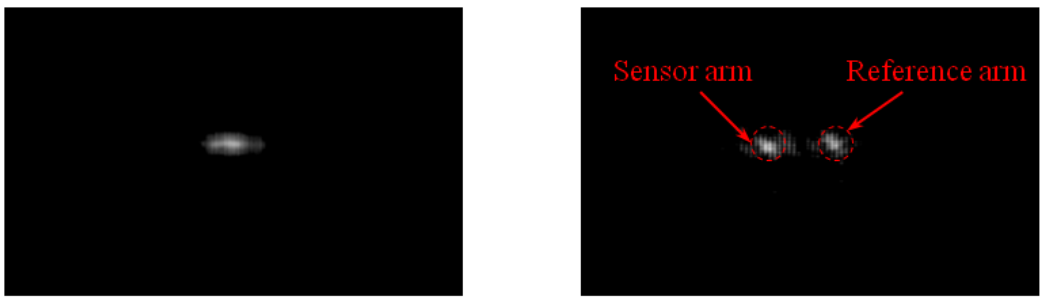

Figure 2.9: CMOS camera images, through a 5X objective, of the output end of (a) the full chip and (b) the mid-section of the chip. The images show a monomode light field. The two bright spots in (b) refers to the light emitting from the reference and the sensor arms of the MZI chip.

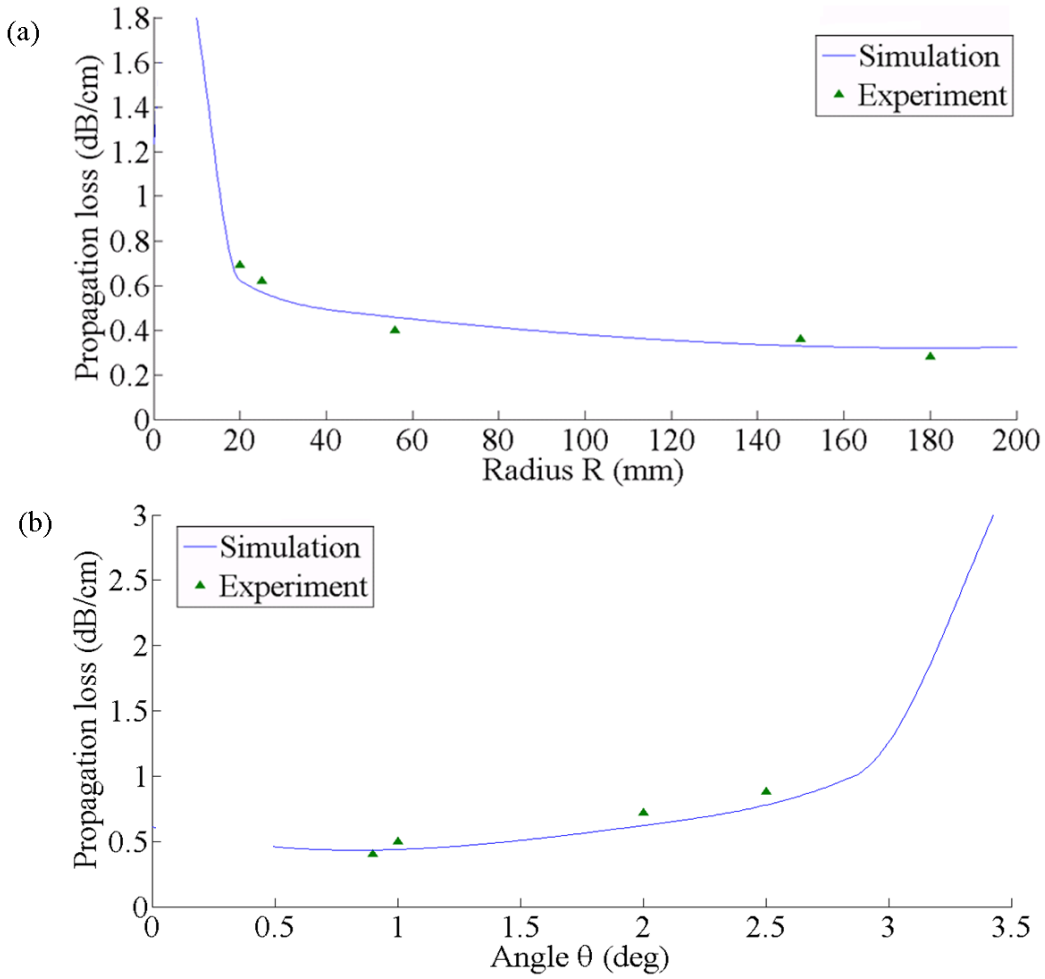

Figure 2.10: (a) The variation of propagation loss with the radius of curvature of Y-junction graph for Sbend MZI, (b) the variation of propagation loss with the angle of Y-junction graph for angular MZI.

References

A. E. Balaev, K. N. Dvoretski, and V. A. Doubrovski. Determination of refractive index of rod-shaped bacteria from spectral extinction measurements. In *Saratov Fall Meeting 2002: Optical Technologies in Biophysics and Medicine IV*, pages 375–380. International Society for Optics and Photonics, 2003.

F. Brosinger, H. Freimuth, M. Lacher, W. Ehrfeld, E. Gedig, A. Katerkamp, F. Spener, and K. Cammann. A label-free affinity sensor with compensation of unspecific protein interaction by a highly sensitive integrated optical mach-zehnder interferometer on silicon. *Sensors and Actuators B: Chemical*, 44(1-3):350–355, 1997.

R. Bruck and R. Hainberger. Polymer waveguide based biosensor. In *Photonics, Devices, and Systems Iv*, pages 71380N–71380N. International Society for Optics and Photonics, 2008.

R. Bruck, E. Melnik, P. Muellner, R. Hainberger, and M. Lämmerhofer. Integrated polymer-based mach-zehnder interferometer label-free streptavidin biosensor compatible with injection molding. *Biosensors and Bioelectronics*, 2011.

S. Chou and P. Krauss. Imprint lithography with sub-10 nm feature size and high throughput. *Microelectronic Engineering*, 35(1):237–240, 1997.

A. Crunteanu, M. Pollnau, G. Jänchen, C. Hibert, P. Hoffmann, R. Salathé, R. Eason, C. Grivas, and D. Shepherd. Ti: sapphire rib channel waveguide fabricated by reactive ion etching of a planar waveguide. *Applied Physics B: Lasers and Optics*, 75(1):15–17, 2002.

D. Esinenco, S. Psoma, M. Kusko, A. Schneider, and R. Muller. Su-8 micro-biosensor based on mach-zehnder interferometer. *Rev. Adv. Mater. Sci*, 10 (4):295–299, 2005.

M. Feit, J. Fleck Jr, et al. Calculation of dispersion in graded-index multimode fibers by a propagating-beam method. *Applied Optics*, 18(16):2843–2851, 1979.

M. Feit, J. Fleck Jr, et al. Computation of mode properties in optical fiber waveguides by a propagating beam method. *Applied Optics*, 19(7):1154–1164, 1980.

R. Forber and E. Marom. Symmetric directional coupler switches. *Quantum Electronics, IEEE Journal of*, 22(6):911–919, 1986.

L. H. Frandsen, P. I. Borel, Y. Zhuang, A. Harpøth, M. Thorhauge, M. Kristensen, W. Bogaerts, P. Dumon, R. Baets, V. Wiaux, et al. Ultralow-loss 3-db photonic crystal waveguide splitter. *Optics letters*, 29(14):1623–1625, 2004.

N. Grote and H. Venghaus. *Fibre optic communication devices*. springer, 2001.

J. Harris, R. Shubert, and J. Polky. Beam coupling to films. *JOSA*, 60(8): 1007–1016, 1970.

R. Heideman and P. Lambeck. Remote opto-chemical sensing with extreme sensitivity: design, fabrication and performance of a pigtailed integrated optical phase-modulated mach-zehnder interferometer system. *Sensors and Actuators B: Chemical*, 61(1-3):100–127, 1999.

R. Heideman, R. Kooyman, and J. Greve. Performance of a highly sensitive optical waveguide mach-zehnder interferometer immunosensor. *Sensors and Actuators B: Chemical*, 10(3):209–217, 1993.

M. Izutsu, Y. Nakai, and T. Sueta. Operation mechanism of the single-mode optical-waveguide y junction. *Optics letters*, 7(3):136–138, 1982.

M. Jonasz, G. Fournier, and D. Stramski. Photometric immersion refractometry: a method for determining the refractive index of marine microbial particles from beam attenuation. *Applied optics*, 36(18):4214–4225, 1997.

D. Jones. *Biomedical Sensors*. Momentum Pr, 2010.

L. M. Lechuga, K. Zinoviev, L. Fernandez, J. Elizalde, O. Hidalgo, and C. Dominguez. Biosensing microsystem platforms based on the integration of si mach-zehnder interferometer, microfluidics and grating couplers. In *SPIE OPTO: Integrated Optoelectronic Devices*, pages 72200L–72200L. International Society for Optics and Photonics, 2009.

A. Liu, L. Liao, D. Rubin, J. Basak, Y. Chetrit, H. Nguyen, R. Cohen, N. Izhaky, and M. Paniccia. Recent development in a high-speed silicon optical modulator based on reverse-biased pn diode in a silicon waveguide. *Semiconductor Science and technology*, 23(6):064001, 2008.

W. Lukosz. Principles and sensitivities of integrated optical and surface plasmon sensors for direct affinity sensing and immunosensing. *Biosensors and Bioelectronics*, 6(3):215–225, 1991.

D. Marcuse. Curvature loss formula for optical fibers. *JOSA*, 66(3):216–220, 1976.

P. Moar, S. Huntington, J. Katsifolis, L. Cahill, A. Roberts, K. Nugent, Y. Iino, P. Davis, G. Margaritondo, G. Tromba, et al. General physics: Nuclear, atomic, and molecular pacs 01 39. *J. Appl. Phys*, 85(7), 1999.

R. Műller, P. Obreja, M. Kusko, D. Esinenco, C. Tibeica, G. Conache, L. Buia, D. Apostol, V. Damian, M. Mateescu, et al. Su 8 used as optical waveguide in integrated optical microsensor for biological applications. In *Advanced Topics in Optoelectronics, Microelectronics, and Nanotechnologies II*, pages 59720Z–59720Z. International Society for Optics and Photonics, 2005.

P. Nellen and W. Lukosz. Integrated optical input grating couplers as direct affinity sensors. *Biosensors and Bioelectronics*, 8(3-4):129–147, 1993.

P. Nellen, K. Tiefenthaler, and W. Lukosz. Integrated optical input grating couplers as biochemical sensors. *Sensors and Actuators*, 15(3):285–295, 1988.

F. W. Olver, D. W. Lozier, R. F. Boisvert, and C. W. Clark. *NIST handbook of mathematical functions*. Cambridge University Press, 2010.

B. Pal. *Fundamentals of fibre optics in telecommunication and sensor systems*. bohem press, 1992.

O. Parriaux and G. Veldhuis. Normalized analysis for the sensitivity optimization of integrated optical evanescent-wave sensors. *Lightwave Technology, Journal of*, 16(4):573–582, 1998.

F. Prieto, B. Sepulveda, A. Calle, A. Llobera, C. Domínguez, A. Abad, A. Montoya, and L. Lechuga. An integrated optical interferometric nanodevice based on silicon technology for biosensor applications. *Nanotechnology*, 14:907, 2003.

A. Rickman, G. Reed, and F. Namavar. Silicon-on-insulator optical rib waveguide loss and mode characteristics. *Lightwave Technology, Journal of*, 12 (10):1771–1776, 1994.

A. Rohrbach. Observing secretory granules with a multiangle evanescent wave microscope. *Biophysical journal*, 78(5):2641–2654, 2000.

R. Scarmozzino, A. Gopinath, R. Pregla, and S. Helfert. Numerical techniques for modeling guided-wave photonic devices. *Selected Topics in Quantum Electronics, IEEE Journal of*, 6(1):150–162, 2000.

B. Sepulveda, J. S. Del Rio, M. Moreno, F. Blanco, K. Mayora, C. Domínguez, and L. M. Lechuga. Optical biosensor microsystems based on the integration of highly sensitive mach–zehnder interferometer devices. *Journal of optics A: pure and applied optics*, 8(7):S561, 2006.

A. Sloper, J. Deacon, and M. Flanagan. A planar indium phosphate monomode waveguide evanescent field immunosensor. *Sensors and Actuators B: Chemical*, 1(1):589–591, 1990.

A. W. Snyder and J. Love. *Optical waveguide theory*, volume 190. Springer, 1983.

L. B. Soldano and E. C. Pennings. Optical multi-mode interference devices based on self-imaging: principles and applications. *Lightwave Technology, Journal of*, 13(4):615–627, 1995.

R. Soref and J. Larenzo. All-silicon active and passive guided-wave components for λ= 1.3 and 1.6 μm. *Quantum Electronics, IEEE Journal of*, 22(6):873–879, 1986.

L. Spiekman, Y. Oei, E. Metaal, F. Green, I. Moerman, and M. Smit. Extremely small multimode interference couplers and ultrashort bends on inp by deep etching. *Photonics Technology Letters, IEEE*, 6(8):1008–1010, 1994.

R. R. Syms and J. R. Cozens. *Optical guided waves and devices*. McGraw-Hill London, 1992.

C. Themistos and B. Rahman. Design issues of a multimode interference-based 3-db splitter. *Applied optics*, 41(33):7037–7044, 2002.

K. Tiefenthaler and W. Lukosz. Sensitivity of grating couplers as integrated-optical chemical sensors. *JOSA B*, 6(2):209–220, 1989.

C. P. Wen. Coplanar-waveguide directional couplers. *Microwave Theory and Techniques, IEEE Transactions on*, 18(6):318–322, 1970.

K. R. Williams, K. Gupta, and M. Wasilik. Etch rates for micromachining processing-part ii. *Microelectromechanical Systems, Journal of*, 12(6):761–778, 2003.

K. Zinoviev, L. G. Carrascosa, J. Sánchez del Río, B. Sepúlveda, C. Domínguez, and L. M. Lechuga. Silicon photonic biosensors for lab-on-a-chip applications. *Advances in Optical Technologies*, 2008, 2008.

Chapter 3

Optical biosensors with an integrated Mach-Zehnder Interferometer for detection of *Listeria monocytogenes* [1]

3.1 Introduction

Listeria monocytogenes is a pathogen found in soil, water, and vegetation that can grow in refrigeration temperatures and can pose a threat to human health. *L. monocytogenes* is a gram-positive, rod-shaped food-borne pathogen that causes listeriosis, which can have a high mortality rate (25 - 30 %) in immune-compromised populations (Aureli et al., 2000; Frye et al., 2002) and pregnant women (Donnelly, 2001; MacDonald et al., 2001). Previously, *L. monocytogenes* outbreaks were mainly reported in seafoods (Embarek, 1994) but the recent outbreaks in ready-to-eat (RTE) meat products (Donnelly, 2001; Schlech and Acheson, 2000) have increased the need for more rapid, sensitive, and selective methods for detection of this bacterium in RTE products. In this paper, we demonstrate an efficient optical immunoassay technique for the detection of *L. monocytogenes*.

Traditionally, the detection of *Listeria* is conducted by culture-based methods, which are time consuming and often labor intensive. Typically, four sequential

[1] A version of this chapter has been submitted for publication in *Biomedical Microdevices*, September 2013, *Under review*

steps are required for culture-based methods of detection - pre-enrichment, selective enrichment, selective plating, and biochemical screening (Chin et al., 2007). The incubation periods can range from several weeks to months, a time frame over which the contaminated RTE meat products would have left the processing plant and already been available to consumers in grocery stores.

Currently, the detection methods for *L. monocytogenes* that are commercially available are assay based, which include enzyme-linked immunosorbent assay (ELISA) (Mattingly et al., 1987), enzyme-linked immunoflourescence assay (ELFA) (Sewell et al., 2003; Ueda and Kuwabara, 2010), fluorescence in-situ hybridization (FISH) (Almeida et al., 2011; Fuchizawa et al., 2009; Moreno et al., 2011), and polymerase chain reaction (PCR) (Kim and Cho, 2010; Kotzekidou, 2013; Omiccioli et al., 2009; Pochop et al., 2012; Shu et al., 2013; Traunšek et al., 2011). Most of these methods need selective enrichment for up to 48 hours. These techniques are laboratory based and are not applicable for real-time identification of *L. monocytogenes* in the field. They also require the use of large quantities of expensive samples and reagents and trained personnel. Hence, there is a real need to develop a technology that will allow rapid, sensitive and cost-effective identification of *Listeria monocytogenes* in food samples.

The use of biosensors for detection of biomolecules has seen rapid progress in the last two decades. Integration of sensors with microelectronics and wireless communication provides high sensitivity, rapid analysis and allows real-time monitoring. Their compatibility with Integrated Circuit (IC) fabrication technologies allows for low-cost large scale fabrication, thus indicating a promising future of biosensors for rapid detection platform. Biosensors use various techniques for the detection of analytes (Griffiths and Hall, 1993; Ivnitski et al., 1999; Leonard et al., 2003; Su et al., 2011), of which label-free optical biosensing technique is widely used due to its simplicity in fabrication, portability, small footprint, low-cost, real-time detection, and high sensitivity (Fan et al., 2008; Marazuela and Moreno-Bondi, 2002).

In this work, a Mach-Zehnder Interferometer (MZI) monomode waveguide

based on total internal reflection (TIR) has been used for label-free optical detection of *Listeria monocytogenes*. The use of MZIs as optical biosensors is rapidly progressing (Bruck et al., 2011; Esinenco et al., 2005; Műller et al., 2005; Sepulveda et al., 2006; Zinoviev et al., 2008) since its first inception by Heideman et al. (1993). In the MZI device, a light beam propagating within the monomodal waveguide is divided into two identical arms (refer Fig. 3.1), the sensor and the reference arms, by means of a Y-junction. After traveling a certain distance (L), the light beam converges, by means of another Y-junction, creating an interference signal. In the sensor arm, a specific area (sensor area) is etched where an electromagnetic field of the propagating light waves, called the evanescent field, can interact with analytes (Brosinger et al., 1997; Marazuela and Moreno-Bondi, 2002; Parriaux and Veldhuis, 1998; Rohrbach, 2000). This interaction causes a change in the effective refractive index of the sensor arm, which will induce a phase difference between the light beams traveling in both arms. This phase difference will depend on the difference of the effective refractive indices of the sensor and the reference arms and on the interaction length (S_l as in Fig. 3.1) of the sensor area.

In a recent work reported by Sarkar et al. (2013), they have demonstrated a systematic approach for the design and fabrication of MZI biosensors with minimum power loss. In their work, they have performed a detailed theoretical and numerical analysis of light field propagation in an MZI waveguide and have quantified the dimensional constraints required for low-loss MZI designs. They have successfully fabricated and tested these low-loss MZI chips showing excellent match between experimental and simulated power losses. The work presented here involves using the fabricated MZI chips reported in (Sarkar et al., 2013) with the entire chip size as small as $1.5mm$ by $30mm$; biofunctionalization of *L. monocytogenes* on the sensor area using a covalent immobilization technique; detection of phase change in the sensor and reference arms through power measurements; determination of limit of detection (LOD) and range of detection (ROD) of the biosensor, and selectivity with respect to other species of bacteria. The novelty of this work is as follows:

a biosensor, highly selective to *Listeria*, has been developed and successfully tested; a new immobilization technique used here has shown highly specific binding of *Listeria* to the sensor area and reduction of the biosensing time; capillary force has been used instead of pumps as a means to transport the biomolecules into the sensor area making the entire system independent of an external power source; and for the first time, an MZI biosensor has been calibrated, using phase change data, which can be used to determine unknown concentrations of bacterial solutions.

3.2 Materials and Methods

3.2.1 Chemicals and Materials

Four inch prime grade polished Silicon wafers were purchased from NanoFab at the University of Alberta, Edmonton, AB. 48% aqueous Hydrofluoric acid (HF) and Sodium bicarbonate ($NaHCO_3$) were obtained from the Chemistry Department at the University of Alberta. Glutaraldehyde (50% aqueous solution), phosphate buffer saline (pH 7.4), 2-aminoethanol or ethanolamine ($\geq$99.5%), isopropanol and ethanol were purchased from Sigma Aldrich, Canada. Freeze-dried *L. monocytogenes* (ATCC strain 43251), unconjugated and FITC tagged rabbit anti-*L. monocytogenes* were provided by Cedarlane®, Burlington, ON, Canada. All solvents used were reagent grade and deionized water (DI-H_2O) was used throughout.

3.2.2 Techniques used

Fabrication of the MZI chips was performed in the NanoFab facility at the University of Alberta, Canada. Characterization of the fabricated chips was carried out using atomic force microscopy (AFM) and ellipsometry. AFM (MFP-3D, Asylum Research, Santa Barbara, CA, USA) was used to measure the dimensions of the fabricated MZI chip. Ellipsometric measurements were used to determine the thickness and refractive index of each layer of the chip using a Sopra GES5E Spectroscopic Ellipsometer (France).

Fluorescent microscopy and scanning electron microscopy (SEM) were used for qualitative study of *L. monocytogenes* functionalization on the chip surface. An inverted fluorescent microscope (Leica DMI6000, Leica Microsystems Inc., ON, Canada) was used to determine the presence of bacteria only on a certain area of the chip (sensor area). SEM (LEO 1430, ZEISS, Germany) was used for imaging the MZI chips to confirm the selectivity of the chip for a given species of the bacteria (*L. monocytogenes*).

Contact angle measurements were performed using a Krüss Drop Shape Analysis System DSA100 (Germany). All measurements were done at room temperature and the values reported are the averages of four separate drops on a given surface.

3.3 Experimental Procedure

3.3.1 Fabrication of MZI chips

The MZI chips were fabricated using nine major steps. The details of the fabrication procedure is already reported elsewhere (Sarkar et al., 2013). A brief summary of the entire procedure is presented here. The general structure, as shown in Fig. 3.1, consists of a silicon substrate <100>, a 1.5 μm thick layer of thermally grown SiO_2 acting as the lower cladding whereas a $2\mu m$ thick layer of chemically deposited (plasma enhanced chemical vapour deposition or PECVD) SiO_2 forms the upper cladding layer. These two layers sandwich a $250nm$ Si_3N_4 core layer deposited by low pressure chemical vapour deposition (LPCVD). The core and cladding layers have a refractive index of 2 and 1.46, respectively, which is ideally suited for total internal reflection (TIR) in a monomode waveguide (Heideman and Lambeck, 1999; Pal, 1992). The MZI configuration was printed on the core layer in the form of a 4 μm x 4 nm ridge structure by a standard photolithographic and reactive ion etching (RIE) technique. Finally, a sensor area was formed by etching through the upper cladding SiO_2 layer ($2\mu m$ deep, $100\mu m$ wide and a varying length, S_l) over a certain area on one of the MZI arms (also called the sensor arm), as shown

in Fig. 3.1. The entire length and width of the chip is $30mm$ and $1.5mm$, respectively. Figure 3.2 shows the SEM image of the $2\mu m$ deep and $100\mu m$ wide cavity, which represents the sensor area. The SEM image provides the cross-sectional area of the MZI chip over which the biofunctionalization will take place. The entire procedure of fabricating the MZI chip is summarized in Fig. 3.3.

Based on the theoretical analysis of the design of MZI structures (Sarkar et al., 2013), ten different MZI configurations were fabricated. These ten different chips can be classified into two broad categories: Angular and Sbend, depending on the shape of the Y-junction divisors of the MZI. The angular MZI is formed with Y-junctions having an opening angle denoted by θ, whereas the Sbend MZI is formed with Y-junctions having circular bends with radii denoted by R. The column 1 of Table 3.1 represents the two different configurations, where A represents the angular Y-junctions and S represents the Sbend Y-junctions. Column 2 represents the opening angle (θ) for angular Y-junctions and radius of curvature (R) for Sbend Y-junctions. The columns 3 and 4 represent the distance between the two arms (d) and length of the arms (L), respectively. The θ values are kept below a certain critical angle ($< 2.5^0$) and the R values kept above a certain critical radius ($> 15mm$) to ensure that the optical losses incurred in the waveguide are with acceptable limits (Sarkar et al., 2013). The columns 5 and 6 represent the length (S_l) and surface area (A_s) of the sensor area, respectively. The last column gives the optical losses for each type of chip, in terms of dB/cm when light from a laser source propagates through them, as measured by a photodiode. For the same sensing length S_l, losses incurred in the Sbend Y-junction designs were much lower than their angular Y-junction counterparts. This can be attributed to the more gradual wave guiding approach of the Sbend design.

There are two deciding factors when it comes to selecting an MZI design for biosensing, namely (i) the optical losses and (ii) the area of sensing. From Table 3.1, it can be clearly seen that $S1$ ($R = 180mm$) is the best design in terms of lowest optical losses. However, the area of sensing is quite low com-

pared to other designs ($1mm^2$). For high sensitivity biosensing experiments, an optimal design is required which would have a larger sensing area with low optical losses. Hence, for the experiments performed in the present work, the $S3$ design of the Sbend configuration was chosen. It has a large sensing area (50% greater than $S1$) yet has an acceptable level of optical losses ($0.4dB/cm$).

3.3.2 Immobilization of *L. monocytogenes* on the sensor area

An immobilization protocol was developed in our laboratory (Micro & Nanoscale Transport Laboratory, University of Alberta) to selectively bind the bacterial cells to the sensor area of the MZI chip only. Silicon dioxide covers almost 97% area of the chip surface with only 3% being the silicon nitride sensor area. Therefore, a procedure was required to create more affinity of *L.monocytogenes* towards the silicon nitride surface (open sensor area) as compared to the silicon dioxide surface (rest of the chip area). This was achieved by the following steps, outlined here.

HF treatment

The fabricated MZI chips were cleaned in a piranha solution (3 parts H_2SO_4 and 1 part H_2O_2) for 15 mins to remove all the organic impurities from the surface. Following that, the chips were rinsed in DI-H_2O and blow-dried with a nitrogen gun. Then, the chips were dipped in a 1% HF solution for 3 minutes and rinsed thoroughly with DI-H_2O. The piranha clean creates a native oxide layer on the silicon nitride surface (Menon and Donovan, 1993) which is removed by the HF treatment (Bañuls et al., 2010; Williams and Muller, 1996).

Modification of surface with glutaraldehyde

The HF treatment performed in the previous step also enhances the concentration of amine (N-H) groups on the Si_3N_4 surface (Cattaruzza et al., 2004; Karymov et al., 1995). The freshly treated chips were then immediately immersed in a 5% glutaraldehyde solution for 90 mins in a nitrogen atmosphere

at room temperature. During this step, glutaraldehyde reacts with the amine groups (present only on the silicon nitride surface) generating aldehyde groups. The chips are then washed thoroughly in DI-H_2O and phosphate buffer saline (PBS) to remove any excess glutaraldehyde before drying them with a nitrogen gun.

Contact angle measurements, performed on silicon nitride surface, showed an increase in water contact angle from 30 ± 2^0 to 48 ± 4^0 (refer Fig. 3.4(a)) after being treated with glutaraldehyde whereas silicon dioxide surface treated with glutaraldehyde following a similar protocol showed an unaltered value for the contact angle (18 ± 1^0) (refer 3.4(b)). This indicates that the glutaraldehyde crosslinkers are anchored exclusively to the amine groups of the silicon nitride (sensor area) portion of the chip.

Immobilization of L. monocytogenes

Unconjugated rabbit anti-*L. monocytogenes* antibody ($0.1 mg/ml$) was added to the glutaraldehyde treated chips and incubated for 30 mins at room temperature. During this period, the aldehyde groups covalently bond with the primary amine of the antibodies. After this period, to prevent any unspecific binding, the unbound aldehyde groups were blocked with 0.1 M ethanolamine for 15 mins at room temperature. The MZI chips were then incubated for 30 mins with increasing concentrations of *L. monocytogenes* in brain heart infusion (BHI) broth solutions ($2.8 \times 10^3 cfu/ml$ to $2.8 \times 10^{13} cfu/ml$). Finally, the chips were rinsed and sonicated in PBS to prevent non-specific binding of cells and then washed with DI-H_2O and blown dry with nitrogen. The schematic representation of surface modification and immobilization is shown in Fig. 3.5. To confirm the specificity of the immobilization procedure, FITC tagged rabbit anti-*L. monocytogenes* antibodies ($0.1\ mg/ml$) was added after the last step. After rinsing the surfaces with PBS and blow drying, they were observed under an inverted fluorescence microscope. Figure 3.6(a) shows the fluorescent image of the silicon nitride surface whereas Fig. 3.6(b) shows the fluorescent image of the silicon dioxide surface. The presence of bacteria only on the

silicon nitride surface is clearly visible from these microscopy images, which again confirms the specific binding of *Listeria* to the sensor area.

Scanning electron microscopy

Selectivity of the surface modified MZI chips was analyzed by SEM imaging. Two MZI chips were prepared with glutaraldehyde and antibodies, as described in the previous subsections. One of the chips was incubated with a 10^9 cfu/ml *L. monocytogenes* solution for 30 mins while the other was incubated with a 10^9 cfu/ml *E. coli* solution for 30 mins. After that, both the chips were rinsed with PBS and DI-H_2O but not dried. To preserve the shape of the bacteria for SEM images, the cells are dehydrated in a graded series of ethanol (30%, 50%, 70%, 80%, 90%, 96% and 100%) and then dried in a critical point drier (CPD). Bacteria contain high proportions of water in their cells and thus, when they are placed in a high vacuum SEM chamber, the water readily evaporates. During evaporation, large surface tension forces are created which leads to the collapse of the bacterial cells. The critical point of a liquid-gas system represents the temperature and pressure above which the phase boundary between the liquid and gas disappears (Heady and Cahn, 1973) and thus the devastating effects of surface tension forces cease to exist. However, the critical point of water is quite high (374^0C, $229bar$) and can destroy the bacterial cells. To overcome this problem, water can be replaced by liquid carbon dioxide (LCO_2), whose critical point is at 31^0C and $74bar$ and does not damage bacterial samples. The graded ethanol series dehydration was performed prior to the CPD step in order to replace all the water in the bacterial cells with ethanol since LCO_2 is miscible with ethanol and not with water. Finally, during the critical point drying step, the LCO_2 is evaporated by maintaining its critical temperature and decreasing the pressure. The chips are then mounted on an SEM stub and sputter-coated with gold before placing it in the SEM chamber for imaging (Gunda et al., 2013). Figure 3.7(a) show the SEM image of one *L. monocytogenes* bacterial cell with its shape preserved by critical point drying. Figures 3.7(b) and (c) show the SEM images of the sensor

area of MZI chips incubated with *L. monocytogenes* and *E. coli*, respectively. These figures clearly show that the MZI chips are selective only to a given species of bacteria (*L. monocytogenes*).

3.3.3 Power measurements

The MZI chips were polished in a custom made waveguide polisher from Ultratec Manufacturing, Inc. and were placed on a piezo-controlled XYZ stage with a minimum resolution of 20 nm. Light from a He-Ne laser ($633nm$) was coupled into the core layer of the chip using a 40X objective lens. The light emanating from the chip was collected by a photodiode. No optical fibers were used in this experiment either to couple the laser light into the chip or collect the light at the output end of the chip. Optical fibers are prone to losses and hence the exclusion of such fibers can increase the efficiency of the device. However, the exclusion of fiber optics makes alignment of the optical components very difficult. For this reason, two complementary metal-oxide-semiconductor (CMOS) cameras have been used for the alignment of the laser-chip system. An overhead camera is placed directly above the chip to monitor the lateral alignment of the laser light into the MZI structure. The vertical alignment is monitored by another CMOS camera placed at the output end of the chip parallel to the direction of propagation of light. Once the optical system is aligned, the horizontal camera is replaced with a photodiode giving the corresponding power reading through a digital read-out. Details related to the alignment procedure can be found elsewhere (Sarkar et al., 2013)

As mentioned earlier (refer section 3.1), the interaction of the biomolecules with the evanescent field of the light waves in the sensor arm of the MZI waveguide causes a change in the effective refractive index of the sensor arm which leads to a phase difference between the sensor and reference arms, given by (Boiarski et al., 1993),

$$\Delta\phi = \frac{2\pi}{\lambda} S_l \Delta N_{eff} \tag{3.1}$$

where, $\Delta\phi$ is the phase change between the guided light in the sensor and reference arms, λ is the wavelength and ΔN_{eff} is the change in the effective

refractive index due to the biointeraction. This phase change, in turn, leads to the change in the normalized power output(ratio of output to input power) of the MZI chip, which can be written as (Boiarski et al., 1993),

$$\Delta P = \frac{1 + cos\Delta\phi}{2} \tag{3.2}$$

where,

$$\Delta P = \frac{P_{out}}{P_{in}} \tag{3.3}$$

Here, ΔP is the normalized power output, P_{out} is the output power and P_{in} is the input power of the MZI chip. In this work, we have calculated the normalized power output values for different concentrations of *Listeria* varying from 2.8×10^3 to 2.8×10^{13} cfu/ml by performing power measurements at the input and output end of the MZI chips. All power measurements were done in air and repeated three times for every concentration of *Listeria*.

3.4 Results and Discussion

3.4.1 Reproducibility

The fabrication and biofunctionalization protocols followed are highly reproducible providing similar results every time. However, power readings of different S3 MZI chips with same concentrations of *Listeria* showed a difference in the values of the output power (P_{out}) and input power (P_{in}), respectively. This difference may have been mainly due to changes in the environmental conditions between experiments and/or slight variations in different batches of the fabricated MZIs. To overcome this challenge and to make the power readings reproducible, a normalized power output scheme has been used (refer 3.3) to nullify the effect of the aforementioned variations.

3.4.2 Results

Fabrication, surface modification, and biofunctionalization of $S3$ MZI chips were carried out according to the procedure mentioned in the previous sections. Prior to power measurements with bacteria, a negative control was

introduced in order to verify that the change in signal was indeed only due to the immobilization of bacteria on the MZI chip. The negative control implies that power measurements were taken after the antibody bonding step and before the *L. monocytogenes* biofunctionalization. This was done for every MZI chip used in the experiments and it gave a constant reading (refer Fig. 3.8).

Figure 3.8 illustrates the variation in the normalized power output of the chip with change in concentration of *L. monocytogenes*. It can be seen that the normalized power intensity increases with the increase in microbial concentration. In general, a higher concentration of bacteria would result in a better surface coverage of the sensor area.

Figure 3.8 also reveals that the output power has a significant intensity as compared to the control even when the bacterial concentration is as low as 2.8×10^5 cfu/ml, which is well below the infective dosage of *L. monocytogenes*. On decreasing the concentration even further, no significant power intensity was detected. Therefore, the limit of detection (LOD) for this biosensor is in the order of 10^5 cfu/ml. The LOD of this device has the potential of reducing to much lower values by using better quality antibodies as it has been reported by others that the quality of antibodies highly affects the sensitivity of the biosensor (Tims et al., 2001).

Another important parameter that has been used to characterize this biosensor is its range of detection (ROD). From Fig. 3.8, it is evident that beyond 2.8×10^{10} cfu/ml, the normalized power intensity value is constant and does not increase with the increase in *L. monocytogenes* concentration. This follows the Langmuir adsorption isotherm which relates the fraction of the surface covered (Θ_A) with concentration of the biomolecule solution, at a given temperature. In this case, the MZI sensor area is entirely covered ($\Theta_A = 1$) at 10^{10} cfu/ml concentration of *L. monocytogenes*. Hence the ROD of this device is from 10^5 cfu/ml to 10^{10} cfu/ml.

In order to determine the selectivity of the MZI biosensor, similar power measurement tests were performed on $S3$ MZI chips with *Escherichia coli*. All surface modification steps were kept the same except for the *L. monocytogenes*

immobilization step. Instead, two different batches of bacterial solutions were added on separate MZI chips. One batch of solutions contained *E. coli* with concentrations varying between 10^5 cfu/ml and 10^{10} cfu/ml while the other batch contained a mixture of *L. monocytogenes* and *E. coli* (1:1 by volume). The latter batch is prepared by mixing a fixed concentration of E. coli (10^9 cfu/ml.) with varying concentrations of L. monocytogenes (2.8×10^5 cfu/ml - 2.8×10^9 cfu/ml) Figure 3.9 illustrates the variation of normalized power intensity with the change in concentration of *E. coli* and the mixture of *E. coli* and *L. monocytogenes*, respectively. It can be seen that the *E. coli* alone does not produce any power signal above the control whereas the *L. monocytogenes* and *E. coli* mixture produces a detectable power, which exceeds the control. However, MZI chips containing a mixture of *L. monocytogenes* and *E. coli* showed lower values of ΔP compared to the MZI chips containing only *L.monocytogenes* for the same values of concentration of *Listeria* (see Figs. 3.8 and 3.9). This was due to the dilution caused by the *E. coli* solution. Another probable reason may be the interference in binding of *L. monocytogenes* cells due to presence of *E. coli*. However, these results clearly show that the output signal is due to *L. monocytogenes* alone and that the fabricated MZI biosensor is highly selective to *L. monocytogenes*.

Figure 3.10 represents the variation of phase change, calculated from Eq. 3.2 for a known value of ΔP, with the change in concentration of *L. monocytogenes* within the range of detection. A third order polynomial fit to the data points ($R^2 = 0.9996$) is done. It provides the variation of the phase change with respect to concentration of *L. monocytogenes*. This can be used as a calibration curve for the MZI chip and can therefore be used as a guide to estimate the value of an unknown concentration of *L. monocytogenes* in a given sample from its phase change value obtained from experiments.

3.5 Conclusion

In this paper, we have demonstrated a Mach-Zehnder Interferometer with the capability to detect *Listeria monocytogenes*. Ten different MZI Y-junction

designs were investigated and an optimum design ($S3$) with a large sensor area ($1.5mm^2$) and low optical losses ($0.4dB/cm$) was chosen for experiments. A specific biofunctionalization protocol was used where, surface treatment of silicon nitride surface with HF greatly reduced the time of antigen immobilization as compared to other traditional methods which use 3-Aminopropyl triethoxysilane (APTES) to create amine groups on the surface. SEM analysis of MZI chips incubated with *L. monocytogenes* and *E. coli* demonstrated the selectivity of the biosensor to *L. monocytogenes*. Power measurements were performed to determine the limit of detection (LOD) and range of detection (ROD) of the fabricated MZI. The LOD of the device is in the order of $10^5 cfu/ml$, which is lower than the infection dosage of *Listeria*. Experimental results also showed that the normalized power output of the MZI biosensors increased with the increase in concentration of the *L. monocytogenes* microbial solution, however, addition of *E. coli* had no such effect confirming the high selectivity of the device to *L. monocytogenes*. Finally, the MZI biosensor was calibrated using phase change data, which can be used to determine unknown concentrations of *L. monocytogenes*. With further developments, this MZI biosensor can be utilized in real-time detection of *L. monocytogenes* directly from ready-to-eat food products available in the market.

Table 3.1: Different configurations of the fabricated MZI chips

Y-junction Design	$\theta(deg)$ for angular/ $R(mm)$ for Sbend	Distance d (μm)	Length of arm $L(\mu m)$	Length of sensor area $S_l(mm)$	Surface area of sensor area $A_s(mm^2)$	Propagation losses (db/cm)
Angular						
A1	0.9	80	16	12	1.2	0.40
A2	1	100	14	10	1.0	0.50
A3	2	100	20	15	1.5	0.72
A4	2	80	21	15	1.5	0.72
A5	2.5	80	22	16	1.6	0.88
Sbend						
S1	180	100	14	10	1.0	0.28
S2	150	80	16	12	1.2	0.36
S3	56	80	20	15	1.5	0.40
S4	25	80	22	16	1.6	0.62
S5	20	100	22	16	1.6	0.69

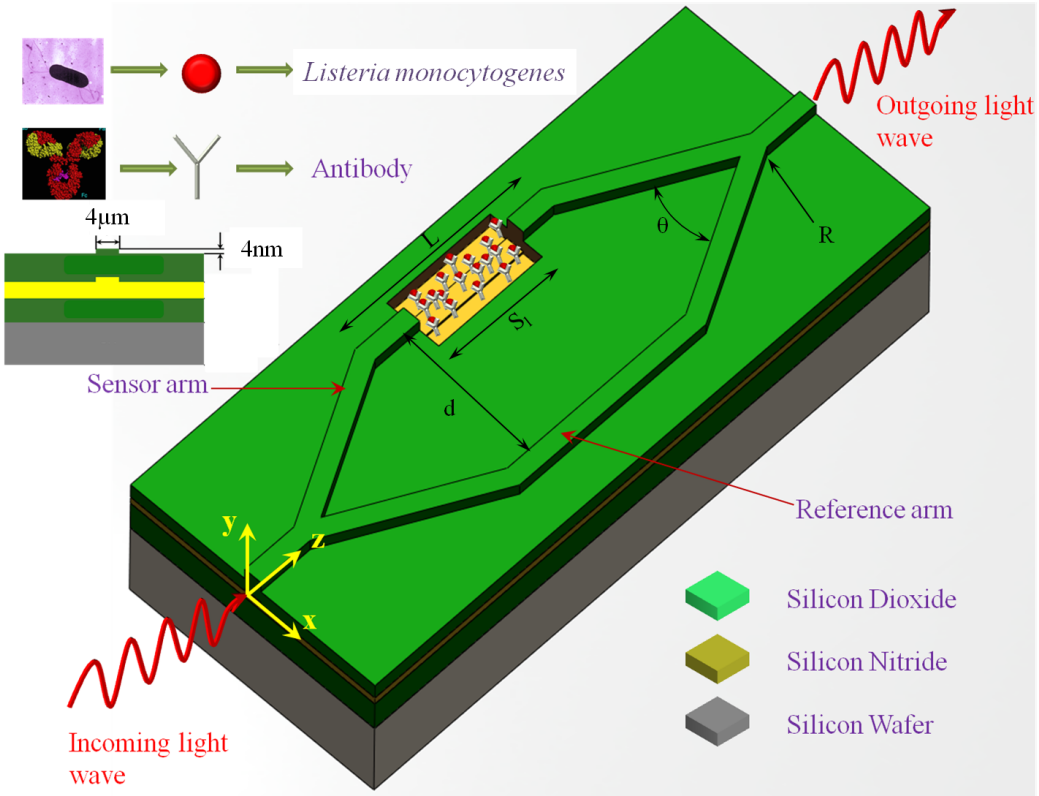

Figure 3.1: Schematic representation of biofunctionalization on MZI. Here, S_l is the length of the sensor area, L is the length of the sensor arm, d is the distance between the sensor and reference arms and θ is the opening angle of the Y-divisor for angular Y-junctions, whereas R is the radius of curvature of the Y-divisor for Sbend Y-junctions.

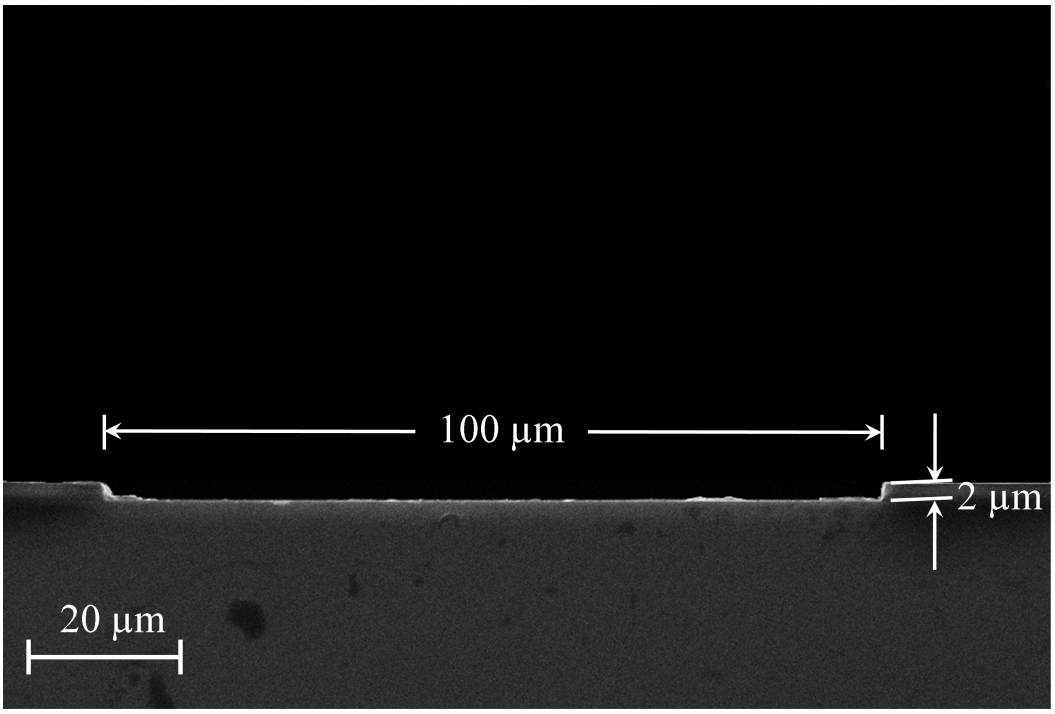

Figure 3.2: SEM image of cross-section of sensing area of the fabricated MZI chip.

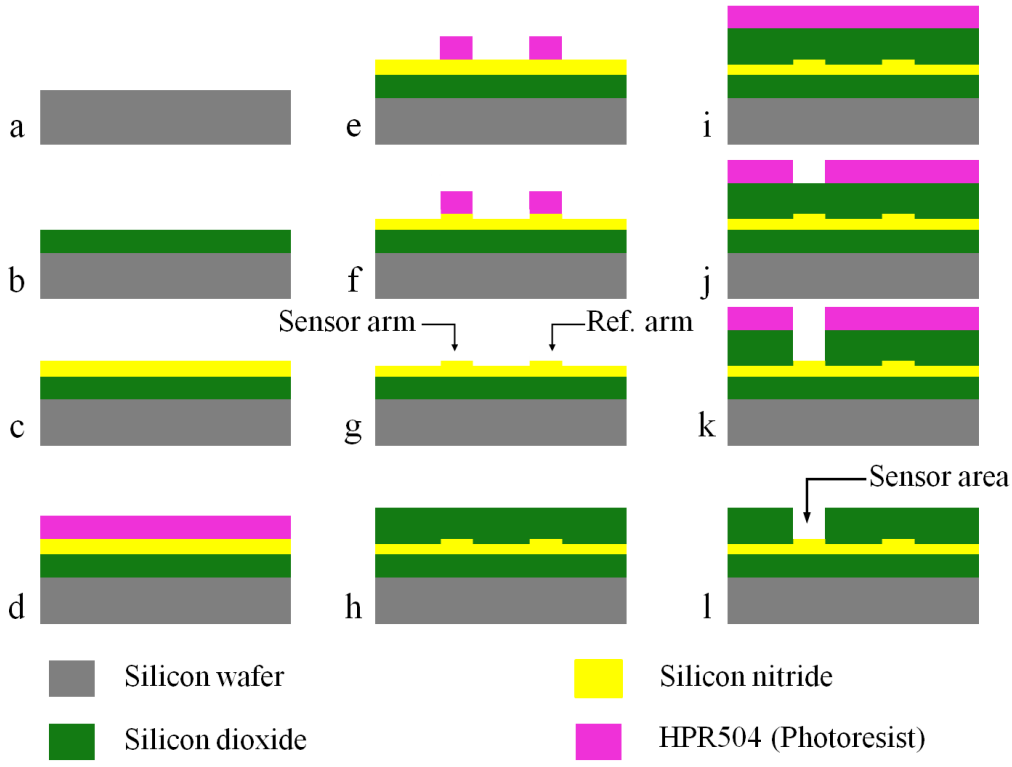

Figure 3.3: Schematic of the fabrication procedure at cross-section of the chip. It involves a. bare silicon wafer, b. thermal oxidation of silicon dioxide on the silicon wafer forming the lower cladding, c. LPCVD of silicon nitride core layer, d. photoresist (HPR504) spinning on the silicon nitride layer, e. photolithography defining the MZI configuration, f. RIE of 4nm depth printing the MZI configuration, g. resist stripped revealing the sensor and reference arms, h. PECVD of silicon dioxide forming the upper cladding, i. HPR504 photoresist spinning on the silicon dioxide layer, j. photolithography defining the sensor area, k. RIE of upper cladding creating the sensing area and l. resist stripped revealing the entire MZI biosensor chip.

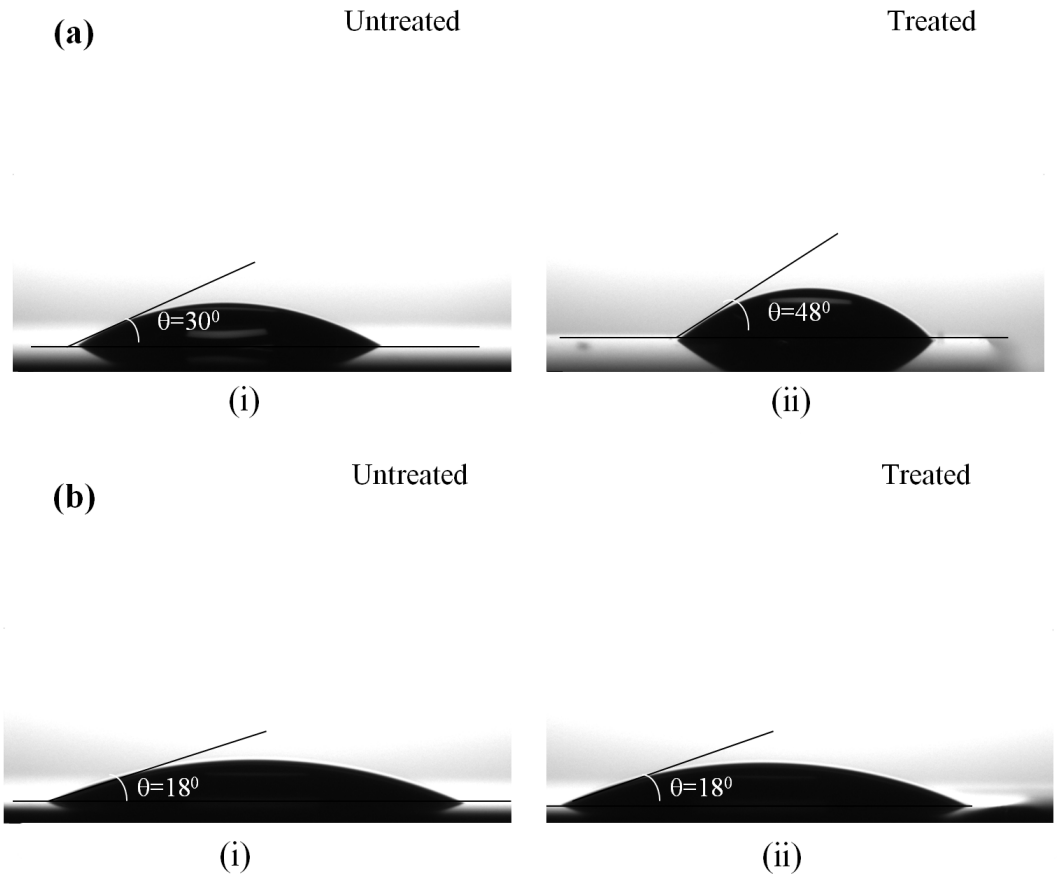

Figure 3.4: (a) Contact angle measurements of silicon nitride surface (i) bare and (ii) treated with glutaraldehyde; (b) Contact angle measurements of silicon dioxide surface (i) bare and (ii) treated with glutaraldehyde.

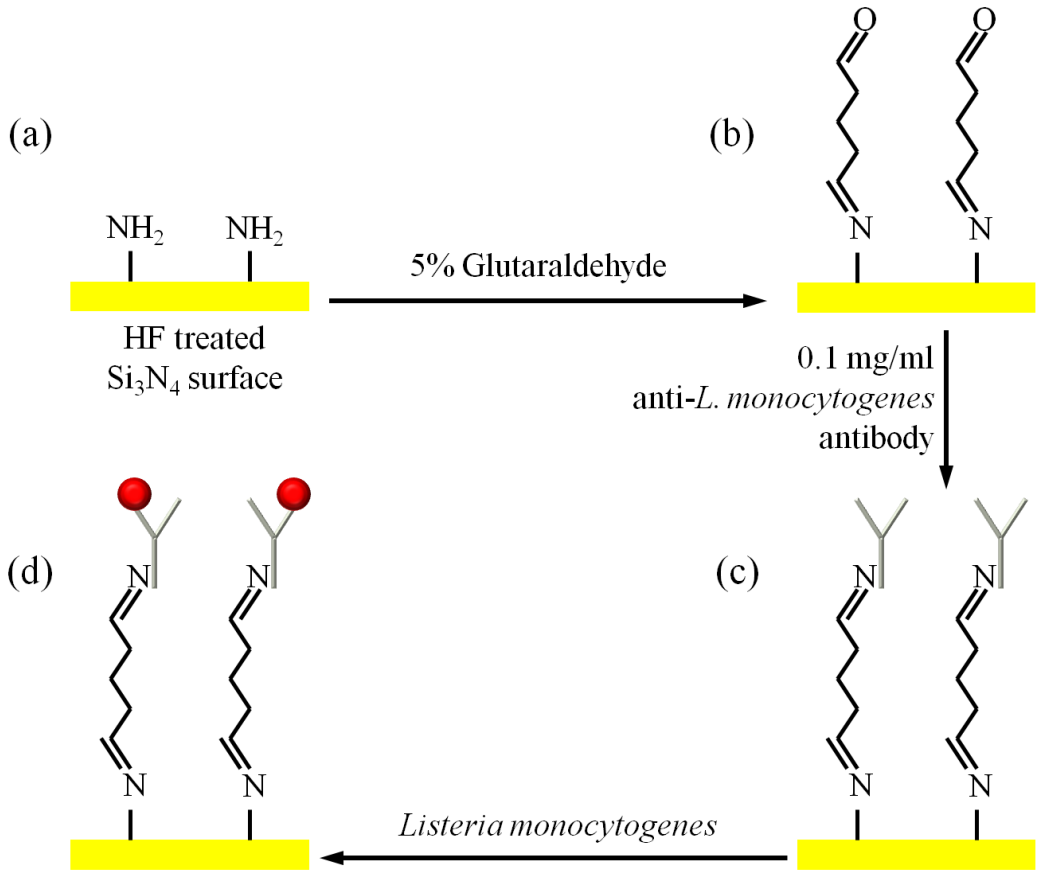

Figure 3.5: Schematic representation of immunoassay procedure on silicon nitride sensing area. (a) Amine groups activated by HF on silicon nitride surface, (b) 5% glutaraldehyde treatment, (c) covalent bonding of antibodies with the aldehyde groups of glutaraldehyde and (d) *Listeria monocytogenes* captured by the antibodies. (The figure is not in scale. The actual size of *Listeria* is much larger than the antibodies.)

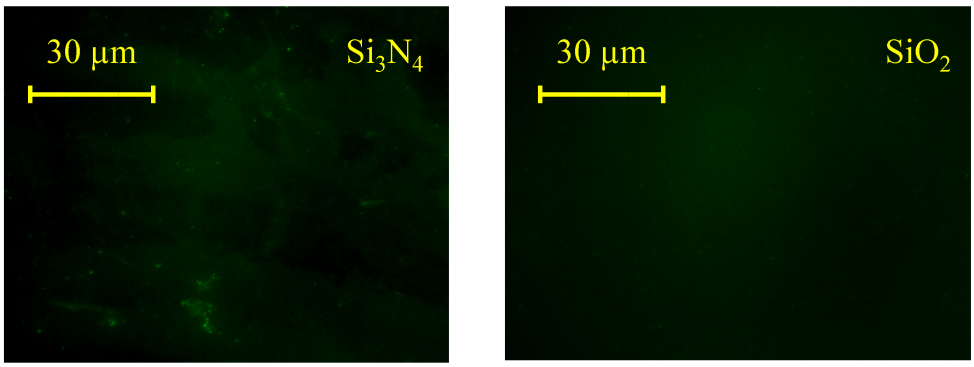

Figure 3.6: Fluorescence microscope images of (a) surface treated silicon nitride surface showing bacterial cells and (b) surface treated silicon dioxide surface devoid of bacterial cells.

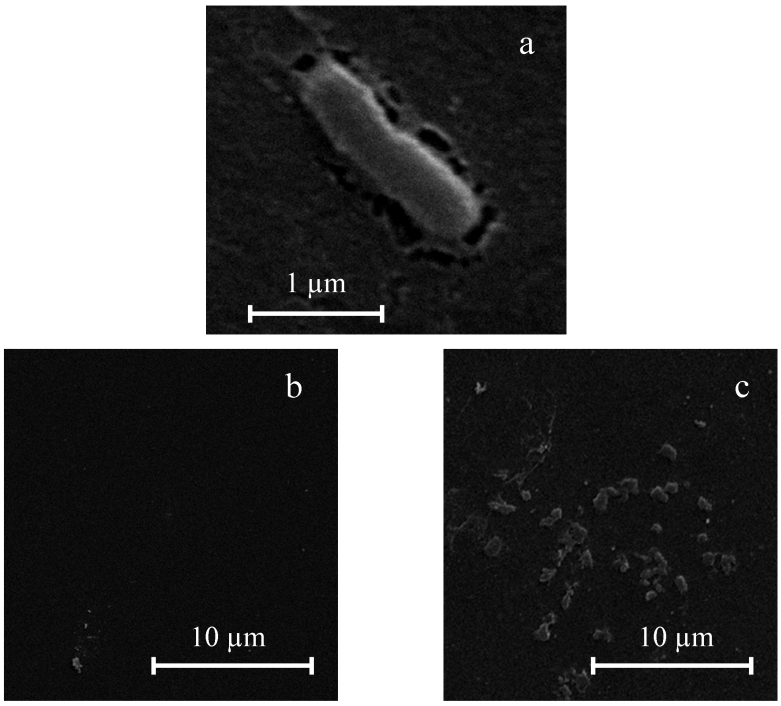

Figure 3.7: SEM images of (a) a single rod-shaped *Listeria monocytogenes* cell, (b) sensor area incubated with *E. coli* and (c) sensor area incubated with *L. monocytogenes*

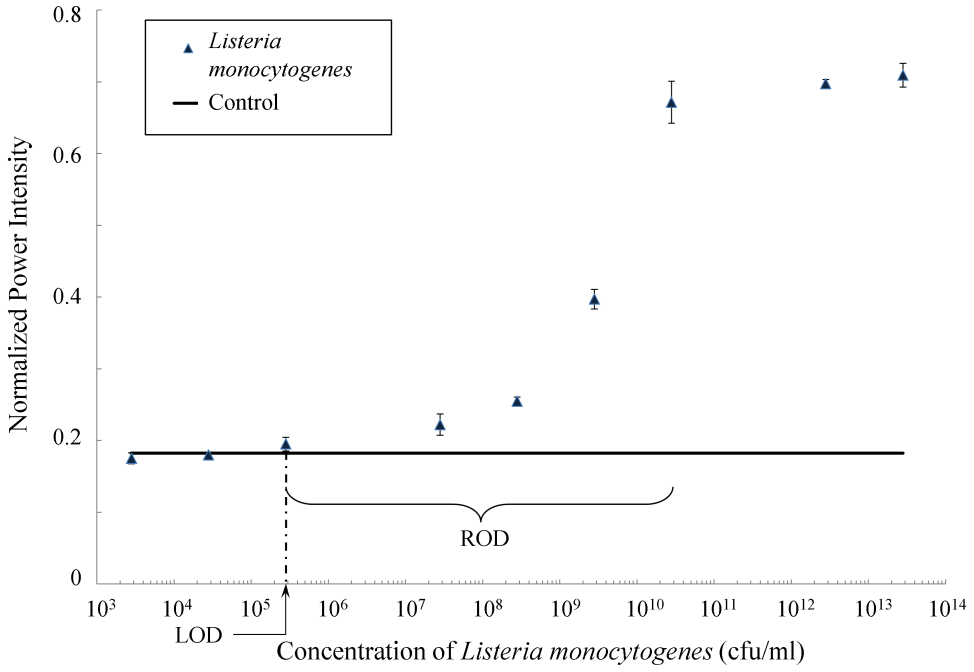

Figure 3.8: Variation of output power with increase in concentration of *Listeria*. The control represents the output power of the biosensor after the antibody bonding step and before the *L. monocytogenes* biofunctionalization.

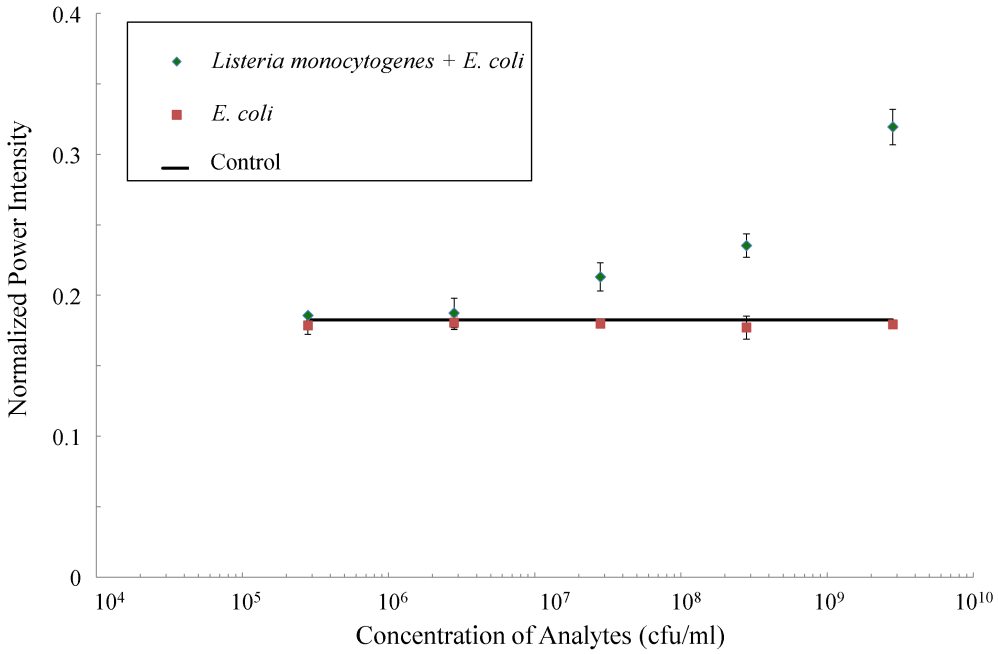

Figure 3.9: Variation of output power with increase in concentration of analytes. The red squares indicate only *E. coli* in the analyte solution for which the horizontal axis represents the concentration of *E. coli*. The green diamond shapes indicate mixture of *E. coli* and *L. monocytogenes* in 1:1 ratio for which the horizontal axis represents the concentration of *Listeria*.

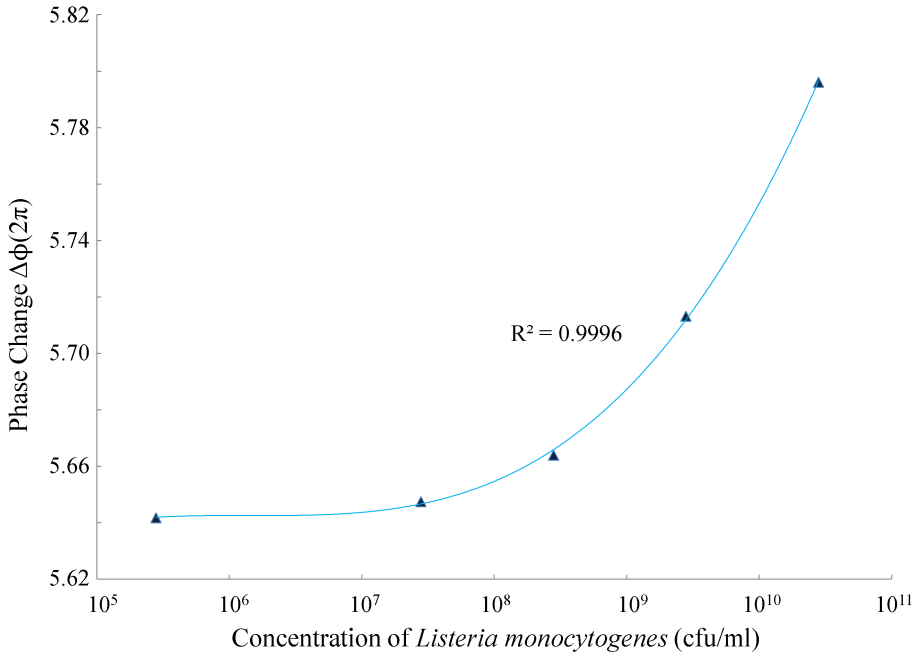

Figure 3.10: Variation of phase change, calculated from Eq. 3.2 for a known value of ΔP, with increase in concentration of *Listeria* within the range of detection (ROD).

References

C. Almeida, N. F. Azevedo, S. Santos, C. W. Keevil, and M. J. Vieira. Discriminating multi-species populations in biofilms with peptide nucleic acid fluorescence in situ hybridization (pna fish). *PLoS One*, 6(3):e14786, 2011.

P. Aureli, G. C. Fiorucci, D. Caroli, G. Marchiaro, O. Novara, L. Leone, and S. Salmaso. An outbreak of febrile gastroenteritis associated with corn contaminated by listeria monocytogenes. *New England Journal of Medicine*, 342(17):1236–1241, 2000.

M.-J. Bañuls, V. González-Pedro, C. A. Barrios, R. Puchades, and Á. Maquieira. Selective chemical modification of silicon nitride/silicon oxide nanostructures to develop label-free biosensors. *Biosensors and Bioelectronics*, 25(6):1460–1466, 2010.

A. A. Boiarski, J. R. Busch, B. S. Bhullar, R. W. Ridgway, and V. E. Wood. Integrated optic sensor with macro-flow cell. *Fibers' 92*, pages 199–211. International Society for Optics and Photonics, 1993.

F. Brosinger, H. Freimuth, M. Lacher, W. Ehrfeld, E. Gedig, A. Katerkamp, F. Spener, and K. Cammann. A label-free affinity sensor with compensation of unspecific protein interaction by a highly sensitive integrated optical mach-zehnder interferometer on silicon. *Sensors and Actuators B: Chemical*, 44(1-3):350–355, 1997.

R. Bruck, E. Melnik, P. Muellner, R. Hainberger, and M. Lämmerhofer. Integrated polymer-based mach-zehnder interferometer label-free streptavidin

biosensor compatible with injection molding. *Biosensors and Bioelectronics*, 26(9):3832–3837, 2011.

F. Cattaruzza, A. Cricenti, A. Flamini, M. Girasole, G. Longo, A. Mezzi, and T. Prosperi. Carboxylic acid terminated monolayer formation on crystalline silicon and silicon nitride surfaces. a surface coverage determination with a fluorescent probe in solution. *Journal of Materials Chemistry*, 14(9):1461–1468, 2004.

C. D. Chin, V. Linder, and S. K. Sia. Lab-on-a-chip devices for global health: past studies and future opportunities. *Lab on a Chip*, 7(1):41–57, 2007.

C. W. Donnelly. Listeria monocytogenes: a continuing challenge. *Nutrition Reviews*, 59(6):183–194, 2001.

P. K. B. Embarek. Presence, detection and growth of *Listeria monocytogenes*in seafoods: a review. *International Journal of Food Microbiology*, 23(1):17–34, 1994.

D. Esinenco, S. Psoma, M. Kusko, A. Schneider, and R. Muller. Su-8 micro-biosensor based on mach-zehnder interferometer. *Rev. Adv. Mater. Sci*, 10 (4):295–299, 2005.

X. Fan, I. M. White, S. I. Shopova, H. Zhu, J. D. Suter, and Y. Sun. Sensitive optical biosensors for unlabeled targets: A review. *Analytica Chimica Acta*, 620(1):8–26, 2008.

D. M. Frye, R. Zweig, J. Sturgeon, M. Tormey, M. LeCavalier, I. Lee, L. Lawani, and L. Mascola. An outbreak of febrile gastroenteritis associated with delicatessen meat contaminated with listeria monocytogenes. *Clinical Infectious Diseases*, 35(8):943–949, 2002.

I. Fuchizawa, S. Shimizu, M. Ootsubo, Y. Kawai, and K. Yamazaki. Specific and rapid quantification of viable listeria monocytogenes using fluorescence in situ hybridization in combination with filter cultivation. *Microbes and Environments*, (0):0905260092, 2009.

D. Griffiths and G. Hall. Biosensorswhat real progress is being made? *Trends in Biotechnology*, 11(4):122–130, 1993.

N. S. K. Gunda, M. Singh, Y. Purwar, S. L. Shah, K. Kaur, and S. K. Mitra. Micro-spot with integrated pillars (msip) for detection of dengue virus ns1. *Biomedical Microdevices*, pages 1–13, 2013.

R. Heady and J. Cahn. Experimental test of classical nucleation theory in a liquid-liquid miscibility gap system. *The Journal of Chemical Physics*, 58: 896, 1973.

R. Heideman and P. Lambeck. Remote opto-chemical sensing with extreme sensitivity: design, fabrication and performance of a pigtailed integrated optical phase-modulated mach–zehnder interferometer system. *Sensors and Actuators B: Chemical*, 61(1):100–127, 1999.

R. Heideman, R. Kooyman, and J. Greve. Performance of a highly sensitive optical waveguide mach-zehnder interferometer immunosensor. *Sensors and Actuators B: Chemical*, 10(3):209–217, 1993.

D. Ivnitski, I. Abdel-Hamid, P. Atanasov, and E. Wilkins. Biosensors for detection of pathogenic bacteria. *Biosensors and Bioelectronics*, 14(7):599–624, 1999.

M. Karymov, A. Kruchinin, Y. A. Tarantov, I. Balova, L. Remisova, and Y. G. Vlasov. Fixation of dna directly on optical waveguide surfaces for molecular probe biosensor development. *Sensors and Actuators B: Chemical*, 29(1): 324–327, 1995.

H.-J. Kim and J.-C. Cho. Simple and rapid detection of *Listeria monocytogenes* in fruit juice by real-time pcr without enrichment culture. *Food Control*, 21 (10):1419–1423, 2010.

P. Kotzekidou. Survey of listeria monocytogenes, salmonella spp. and escherichia coli o157:h7 in raw ingredients and ready-to-eat products by commercial real-time pcr kits. *Food Microbiology*, 35(2):86–91, 2013.

P. Leonard, S. Hearty, J. Brennan, L. Dunne, J. Quinn, T. Chakraborty, and R. OKennedy. Advances in biosensors for detection of pathogens in food and water. *Enzyme and Microbial Technology*, 32(1):3–13, 2003.

P. MacDonald, R. Whitwam, J. Boggs, J. Reardon, R. Saah, M. Beatty, J. Sobel, L. Graves, S. Hunter, and J. MacCormack. Outbreak of listeria-associated birth complications linked with homemade mexican-style cheese, north carolina, 2000. In *Clinical Infectious Diseases*, volume 33, pages 1236–1236. UNIV CHICAGO PRESS 1427 E 60TH ST, CHICAGO, IL 60637-2954 USA, 2001.

M. Marazuela and M. Moreno-Bondi. Fiber-optic biosensors–an overview. *Analytical and Bioanalytical Chemistry*, 372(5-6):664–682, 2002.

J. Mattingly, B. Butman, M. Plank, R. Durham, B. Robison, et al. Rapid monoclonal antibody-based enzyme-linked immunosorbent assay for detection of listeria in food products. *Journal-Association of Official Analytical Chemists*, 71(3):679–681, 1987.

V. Menon and R. Donovan. Handbook of semiconductor wafer cleaning technology, *Noyes Publication, New Jersey*, 1993.

Y. Moreno, L. Ballesteros, J. García-Hernández, P. Santiago, A. González, and M. A. Ferrús. Specific detection of viable *Listeria monocytogenes* in spanish wastewater treatment plants by fluorescent *in situ* hybridization and pcr. *Water Research*, 45(15):4634–4640, 2011.

R. Műller, P. Obreja, M. Kusko, D. Esinenco, C. Tibeica, G. Conache, L. Buia, D. Apostol, V. Damian, M. Mateescu, et al. Su 8 used as optical waveguide in integrated optical microsensor for biological applications. In *Advanced Topics in Optoelectronics, Microelectronics, and Nanotechnologies II*, pages 59720Z–59720Z. International Society for Optics and Photonics, 2005.

E. Omiccioli, G. Amagliani, G. Brandi, and M. Magnani. A new platform

for real-time pcr detection of *Salmonella* spp., *Listeria monocytogenes* and *Escherichia coli* o157 in milk. *Food Microbiology*, 26(6):615–622, 2009.

B. P. Pal. *Fundamentals of fibre optics in telecommunication and sensor systems*. Bohem Press, 1992.

O. Parriaux and G. Veldhuis. Normalized analysis for the sensitivity optimization of integrated optical evanescent-wave sensors. *Journal of Lightwave Technology*, 16(4):573–582, 1998.

J. Pochop, M. Kačániová, L. Hleba, L. Lopasovskỳ, A. Bobková, L. Zeleňáková, and M. Stričík. Detection of listeria monocytogenes in ready-to-eat food by step one real-time polymerase chain reaction. *Journal of Environmental Science and Health, Part B*, 47(3):212–216, 2012.

A. Rohrbach. Observing secretory granules with a multiangle evanescent wave microscope. *Biophysical Journal*, 78(5):2641–2654, 2000.

D. Sarkar, I. Jamal, and S. K. Mitra. Analysis, design and fabrication of optical waveguides for mach-zehnder interferometry. *Optics Communications*, 311: 338–345, 2013.

W. F. Schlech and D. Acheson. Foodborne listeriosis. *Clinical Infectious Diseases*, 31(3):770–775, 2000.

B. Sepulveda, J. S. Del Rio, M. Moreno, F. Blanco, K. Mayora, C. Domínguez, and L. M. Lechuga. Optical biosensor microsystems based on the integration of highly sensitive mach–zehnder interferometer devices. *Journal of Optics A: Pure and Applied Optics*, 8(7):S561, 2006.

A. Sewell, D. Warburton, A. Boville, E. Daley, and K. Mullen. The development of an efficient and rapid enzyme linked fluorescent assay method for the detection of *Listeria* spp. from foods. *International Journal of Food Microbiology*, 81(2):123–129, 2003.

B. Shu, C. Zhang, and D. Xing. Highly sensitive identification of foodborne pathogenic listeria monocytogenes using single-phase continuous-flow nested pcr microfluidics with on-line fluorescence detection. *Microfluidics Nanofluidics*, 15(2):161–172, 2013.

L. Su, W. Jia, C. Hou, and Y. Lei. Microbial biosensors: a review. *Biosensors and Bioelectronics*, 26(5):1788–1799, 2011.

T. B. Tims, S. S. Dickey, D. R. Demarco, and D. V. Lim. Detection of low levels of listeria monocytogenes within 20 hours using an evanescent wave biosensor. *American Clinical Laboratory*, 20(8):28–31, 2001.

U. Traunšek, N. Toplak, B. Jeršek, A. Lapanje, T. Majstorović, and M. Kovač. Novel cost-efficient real-time pcr assays for detection and quantitation of *Listeria monocytogenes*. *Journal of Microbiological Methods*, 85(1):40–46, 2011.

S. Ueda and Y. Kuwabara. Evaluation of an enzyme-linked fluorescent assay for the detection of listeria monocytogenes from food. *Biocontrol Science*, 15(3):91–95, 2010.

K. R. Williams and R. S. Muller. Etch rates for micromachining processing. *Journal of Microelectromechanical Systems*, 5(4):256–269, 1996.

K. Zinoviev, L. G. Carrascosa, J. Sánchez del Río, B. Sepúlveda, C. Domínguez, and L. M. Lechuga. Silicon photonic biosensors for lab-on-a-chip applications. *Advances in Optical Technologies*, 2008, 2008.

Chapter 4

Conclusion and Future Prospects

4.1 Summary and Concluding Remarks

The present research focuses on the real-time detection of a dangerous food-borne pathogen *Listeria monocytogenes*. A label-free optical biosensor working on the principle of a Mach-Zehnder interferometer was developed for the detection of the bacterium. The steps involved in the development of the biosensor are as follows:

- Design and analysis of an optimal MZI configuration involving low optical losses.
- Development of a reproducible micro/nanofabrication scheme for fabricating the MZI biosensor chips.
- Sample preparation and development of a rapid biomolecule immobilization protocol using Hydrofluoric acid treatment.
- Validation of the sensitivity and selectivity of the biosensor through power measurements and SEM analysis, respectively.
- Interpretation of the experimental results for devising a novel technique for quantifying unknown concentrations of *Listeria monocytogenes*.

Simplicity in fabrication, portability, small footprint, real-time detection and high sensitivity are few of the many advantages of label-free optical sensors.

They work on the principle of evanescent field detection where a small portion of the light waves propagating through waveguide penetrates through the core-cladding interface and propagates parallel to the direction of propagation. The interaction of a biomolecule with the biosensor is captured in this evanescent field and carried to the output end of the biosensor where light intensity measurements determines the biomolecular concentration. Since, these types of biosensors heavily depend on the accuracy of the output signal, monomode waveguides are used to prevent any intermodal dispersion caused by higher order modes. Extensive mode calculations of waveguiding structures have been performed through simulations to design a monomodal low-loss MZI structure. The limiting dimensions for the MZI configuration have also been calculated through both theoretical and experimental results.

Once the afore-mentioned analysis was complete and a final set of designs was realized, a fabrication protocol was developed for quick and easy production of the MZI biosensor chips. The main aim behind developing such a protocol was to have a fabrication system that could be transformed into a mass-production scheme. This was achieved in nine major steps which has been discussed in details in Chapter 2. The fabricated waveguides were tested for optical power losses and the results agreed with the simulation studies. Following this, an MZI chip with low optical losses and a large sensing area was chosen for experiments.

ATCC 43251 strain of *Listeria monocytogenes* was used as the analyte in our experiments. A rapid immobilization technique was developed which involved treatment of the biosensing surfaces with HF and glutaraldehyde. This technique greatly reduced the biomolecule immobilization time compared to traditional techniques (involving the use of APTES), however, its greatest advantage was the specific binding of the bacteria on the sensor area of the biosensor. The sensing area occupies only about 3% of the entire chip surface and specific binding of bacteria to the sensor area ensures a good signal strength at the output, which is nearly impossible with traditional techniques. Power measurements were performed using a set-up described in Chapter 3.

The limit of detection of the MZI biosensor was found to be 2.8×10^5 cfu/ml with the range of detection from 10^5 cfu/ml to 10^{10} cfu/ml. However, the biosensor has the potential of detecting lower concentrations of bacteria with the use of better quality antibodies. SEM images of the sensing area with *L. monocytogenes* and *E. coli*, respectively showed the selective affinity of the biosensor to *L. monocytogenes* only.

A phase change graph was plotted from the power measurements at different concentrations of *Listeria monocytogenes*. It has been proposed that such a phase change plot can be used as a means of quantifying unknown concentrations of the bacterium, in the range of detection.

4.2 Future Work

In this work, an open channel opto-fluidic biosensor with a capillary driven flow has been demonstrated. Further development would involve the integration of a microfluidic network with inlet and outlet reservoirs on the sensor area of the MZI chip. This would facilitate a more systematic and controlled discharge of analyte solutions into the sensing area of the biosensor. The inlet and outlet reservoirs would also allow a number of rigorous washing and cleaning steps which would make the MZI chips reusable. This would also protect the chip form harsh environments and facilitate the use of the chip in the field, outside the controlled environment of the laboratory. However, for the chip to be usable in the field, the entire experimental setup needs to be miniaturized and cased into a single unit which would be portable and robust.

As mentioned previously, the use of very high quality antibodies can increase the sensitivity of the biosensor significantly. Also, with progress in the area of microbial sample preparation, soon this MZI biosensor chip would be able to perform rapid *in-situ* detection of *Listeria monocytogenes* from food products before being available to consumers. Finally, since there are numerous other species of bacteria that pose a threat to human health and safety, accurate calibration systems for the MZI biosensors can be developed with further research to accurately predict the composition of a microbial solution containing

a mixture of several bacterial species.

Appendix

A-1 Detailed fabrication techniques used

We report here the details of the fabrication procedures followed in Chapter 2. Similar procedures were followed in Chapter 3.

A-1.1 Mask Design

The mask for photolithography was designed using a mask generation software from Tanner EDA, L-Edit. The mask consists of a 5x5 *inch* glass plate with a chrome layer deposited on it. A pattern generator then uses the mask design to etch the chrome layer from the glass plate using a laser. The design consists of five Angular Y-junctions with varying opening angles and five Sbend Y-junctions with varying radii of curvature. Each design had three copies separated by 1.5 mm. Two 100 μm wide *locator strips* were placed at the input and output ends of the MZI structure to allow easy location of the nano-dimension ridges. As the ridge is placed exactly at the center of the locator strips, aligning the light source through the ridge would be relatively simple. *Alignment markers* were also placed on various areas of the mask for aligning the mask on the same position as the first lithographic step during the second lithographic step.

A-1.2 Piranha cleaning

A solution with 3 parts H_2SO_4 and 1 part H_2O_2 was used. The bare Si wafers were left in a glass beaker, containing 1 *liter* piranha solution, for 15 minutes. After that the wafers were properly rinsed with DI water for 10 minutes and then blow dried with an N_2 gun.

A-1.3 Thermal oxidation

In order to get a high quality oxide layer with high uniformity to form the lower cladding, thermal oxidation is preferred since it is very important to have maximum uniformity before deposition of Si_3N_4. During thermal oxidation, the oxygen molecules react with the silicon to from silicon dioxide. It is interesting to note that 54% of the final thickness of silicon dioxide is the added thickness; the remaining 46% is due to the conversion of silicon wafer

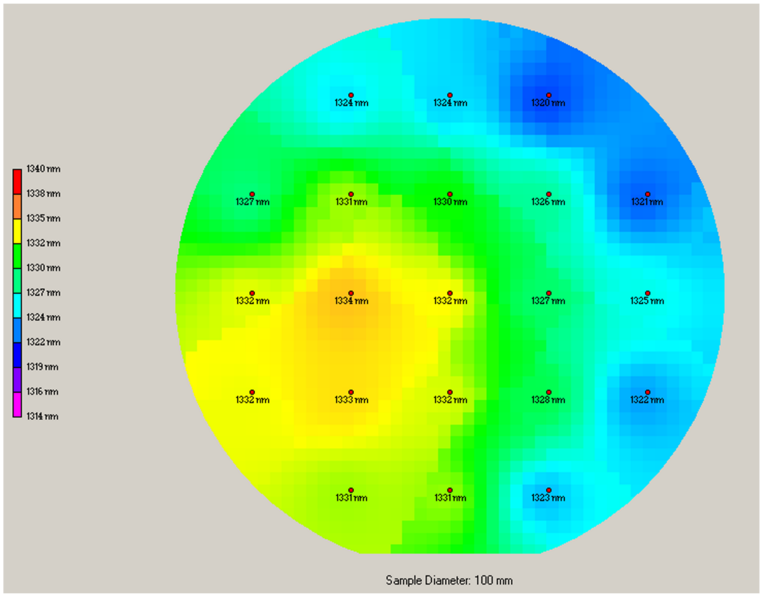

Figure A-1: Thickness of the thermally grown silicon dioxide lower cladding layer at various points on the silicon wafer showing a highly uniform thickness. This measurement was done using *Filmetrics Resist and Dielectric Thickness Mapping System* at the NanoFab facility at the University of Alberta.

to oxide. This is due to the fact that the density of silicon dioxide is lesser than pure silicon meaning greater volume of silicon dioxide.

Wet oxidation technique was used in the fabrication since it is faster and gives a much thicker layer of oxide, of the order of 1.5 μm, as compared to 100 nm by dry oxidation. The chemical reaction that occurs during the wet oxidation process is as follows:

$$Si + 2H_2O \longrightarrow SiO_2 + 2H_2(g)$$

After 8 hours of operation the desired thickness and refractive index of SiO_2 were achieved (as shown in Fig. A-1 and A-2)

A-1.4 LPCVD of Si_3N_4

Low Pressure Chemical Vapor Deposition of Si_3N_4 is performed on the thermally oxidized Si wafer. LPCVD nitride can easily be deposited in a very pure

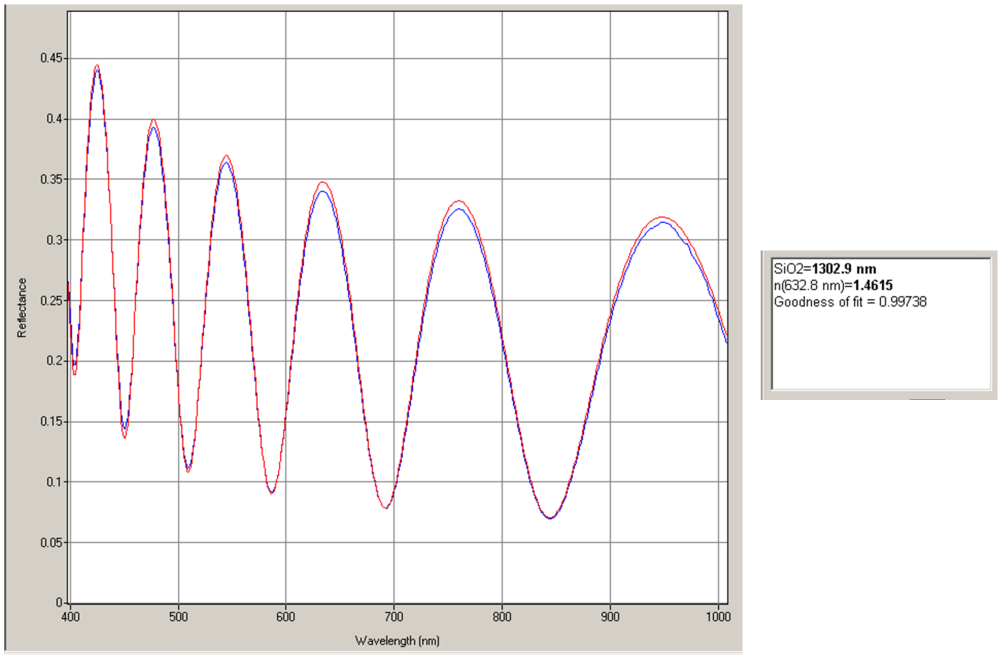

Figure A-2: Refractive index of the thermally grown silicon dioxide lower cladding layer at any given point on the silicon wafer. This measurement was done using *Filmetrics Resist and Dielectric Thickness Mapping System* at the NanoFab facility at the University of Alberta.

and uniform way which leads to high thermal stability and low etch rates. Low etch rate is an essential advantage of LPCVD because it can etch features with depths as small as 4 nm. During LPCVD, a chemical reaction occurs between DCS (dichlorosilane) and ammonia which deposits a layer of Si_3N_4 on the wafer. The reaction is as follows:

$$3SiH_2Cl_2 + 4NH_3 \longrightarrow Si_3N_4 + 6HCl(g) + 6H_2(g)$$

The reaction was maintained at a temperature of 835^{o}C for 52 minutes with a deposition pressure of 250 $mTorr$ which is low enough for a good uniform layer of Si_3N_4. The amount of DCS and ammonia were 100 and 20 $sccm$, respectively.
Figures A-3 and A-4 represent the thickness and refractive index measurements of the core layer. They reveal that the desired values of thickness and refractive index of the core layer have been achieved.

A-1.5 Photolithography of the first layer

Photolithography is arguably the most important step of the whole fabrication process. A positive photoresist, HPR504, was used. There are a couple of reasons why HPR504 was chosen over the commonly used SU-8. Firstly, HPR 504 is a positive photoresist which means the portion of the resist exposed to light becomes soluble in a resist developer and since we have used an inverted mask, a negative photoresist (SU-8) will not serve the purpose. Secondly, SU-8 generates large internal stresses and is very difficult to remove and so was not preferred for a waveguide with sub-micron features.
The whole photolithographic process was completed in several steps. The first step involved dehydrating the wafer inside an oven and flowing HMDS (hexamethyldisilazane) which enhances adhesion of the photoresist onto the wafer. It is to be noted that HMDS does not work on metallic surfaces. In the following step, 5 ml of HPR504 was spread on the wafer in a Solitec Spinner. The resist was first spread at 500 rpm for 10 seconds and then spun at 4000 rpm for 40 seconds. The thickness of the photoresist layer was a little above 1 μm. Next, the resist is baked on a Solitec Vacuum Hotplate at 115^{o}C for 90 seconds. Once the resist perfectly adheres to the substrate, it is placed in a Mask Aligner where the photoresist was exposed to UV light (365 nm) through the mask for 3 seconds. Then the wafer, with the cured photoresist, is developed in 354 developer, which is a solution of 2% NaOH in water, for 20

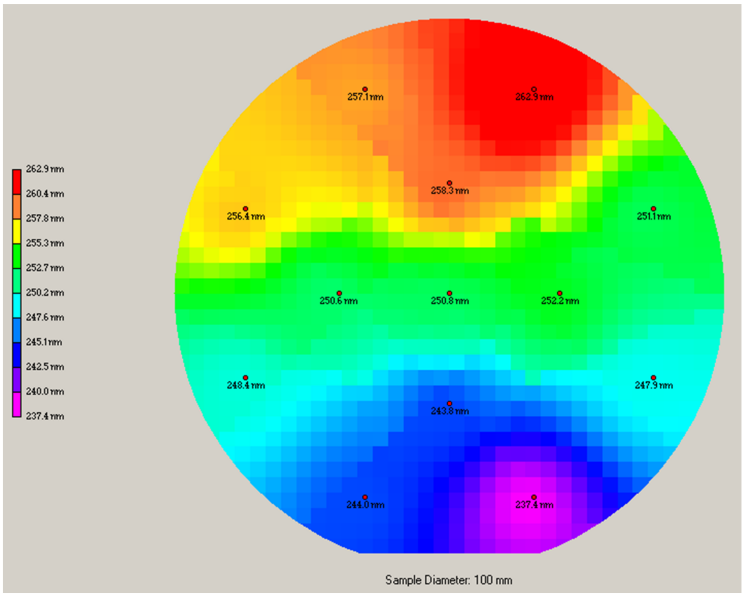

Figure A-3: Thickness of the silicon nitride core layer at various points on the wafer showing an thickness of 250 *nm*. This measurement was done using *Filmetrics Resist and Dielectric Thickness Mapping System* at the NanoFab facility at the University of Alberta.

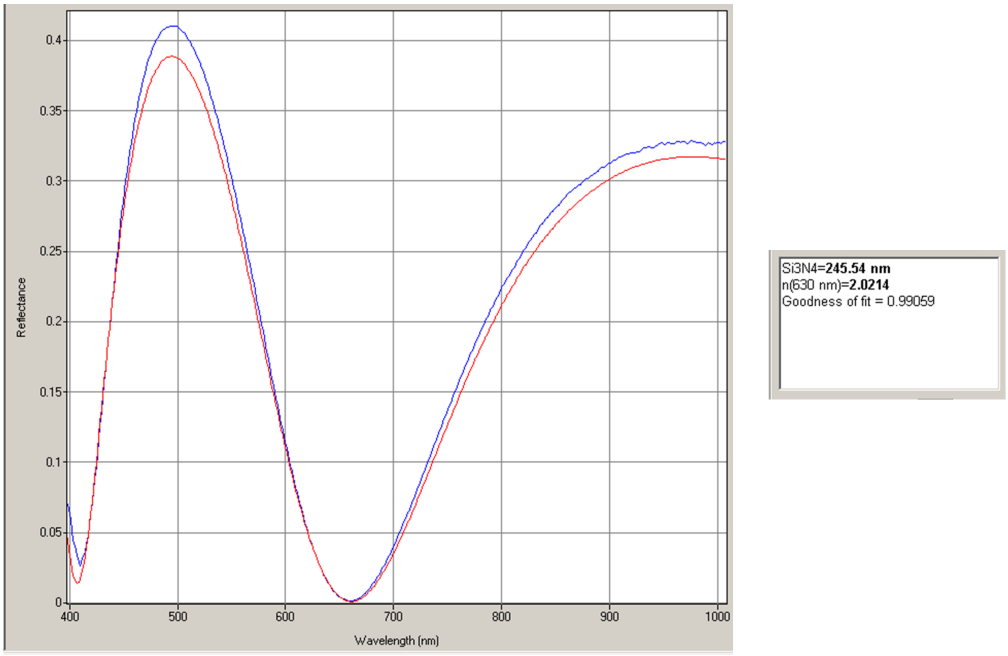

Figure A-4: Refractive index of the silicon nitride core layer at any given point on the wafer. This measurement was done using *Filmetrics Resist and Dielectric Thickness Mapping System* at the NanoFab facility at the University of Alberta.

seconds. It is always a good practice to keep the developing time low and then check the photoresist under a microscope so that if the resist is underdeveloped, one can perform another developing step. If the developing time is too high then the resist might be overdeveloped and the whole procedure will have to be repeated. In the last step, the mask is cleaned and dried in a Photomask Cleaning Station and stored in the clean room for future use.

A-1.6 RIE of the first layer

After the photoresist was deposited on the silicon nitride layer, a Reactive Ion Etching (RIE) step was performed on the substrate in order to make the planar rib structures for the optical waveguide. RIE was preferred since it etches anisotropically and gives vertical sidewalls. Before etching, the RIE chamber was cleaned with oxygen gas (50 $sccm$) for 10 minutes at a pressure of 250 $mTorr$ and rf power of 250 W. The etch rate of the RIE (TRION) equipment used for this purpose was undetermined and so different etch times were selected for etching and then with the help of AFM, the respective etch depths were determined. It was found that for an etch time of 5 seconds, a rib height of 4 nm was achieved. We used the Nitride recipe for etching. During the process, pressure was maintained at 150 $mTorr$ and a radiofrequency (rf) power of 125 W. An optimal rf power was selected because although a higher rf power would mean a higher etch rate, it could damage the sample also. The gases used were CF_4 and O_2, 45 and 5 $sccm$ respectively.
Once the RIE was complete, the resist (HPR504) was removed in two steps. The first step included dipping the wafer into acetone and then washing it with IPA and water and then blow drying. This step removes the bulk of the resist and is called bulk stripping. In the second step, the wafer was put in a Branson Stripper for 10 minutes where the remaining photoresist was removed by O_2 plasma.

A-1.7 PECVD of SiO_2

The upper cladding layer does not demand too much of uniformity but it is very essential that the stress induced by the deposition of a thick upper cladding layer is well controlled. Hence Plasma Enhanced Chemical Vapor Deposition process was used for forming the upper cladding layer. The rate of deposition is high and a thick layer of silicon dioxide can be deposited at low temperatures by PECVD (about 300^oC). If there is too much stress acting

on the substrate due to deposition of a thick layer of SiO_2, it can cause the whole wafer to bend. Hence PECVD is preferred since it can control the stress created due to the deposition.
In PECVD, nitrous oxide reacts with silane to deposit a layer of silicon dioxide on the substrate. The reaction is as follows:

$$3SiH_4 + 6N_2O \longrightarrow 3SiO_2 + 4NH_3(g) + 4N_2(g)$$

The PECVD (TRION) equipment used has a deposition rate of $190nm/250secs$ and therefore a deposition time of 2525 seconds was used. The procedure was also repeated for different times and each time it was seen that the thickness at the center was lower than at the edges. For example, for a deposition time of 1350 seconds, the thickness at the center was 1200-1300 nm whereas at the periphery it was about 1400 nm. The gases used were oxygen and TEOS (Tetraethyl orthosilicate), 85 and 100 $sccm$ respectively, at 300^oC and a pressure of 1015 $mTorr$ and an rf power of 60 W. Figure A-5 reveals that the desired values of thickness and refractive index of the core layer have been achieved.

A-1.8 Photolithography of the second layer

The basic lithographic steps are exactly the same with the only complication being that the mask and the wafer needed to be aligned at exactly the same position as it was in the first lithographic step so that during RIE, the etch is only on the sensor area. This was done with the help of the alignment markers.

A-1.9 RIE of the second layer

This step is similar in procedure to the previous RIE step, the only differences being that an Oxide recipe was used instead of a Nitride recipe and that the etch rate for SiO_2 was around 210 nm/min. Therefore, the total time taken to etch approximately $2.2\mu m$ of SiO_2 was 10.5 minutes.
The resist layer was then stripped off after the RIE. At the end of this step, the wafers were ready to be diced into waveguide chips.

A-1.10 Dicing

Once the wafers were fabricated, they were diced into small 1.5×30 mm chips. This step was completed using a diamond cutter dicing tool. The blade of the

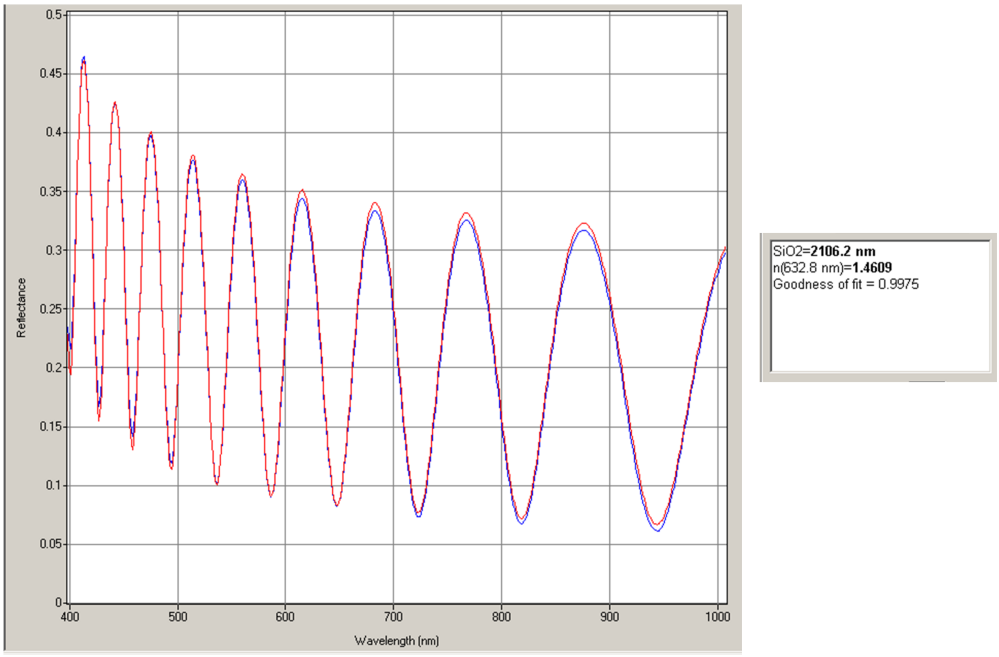

Figure A-5: Average thickness and refractive index of the silicon dioxide upper cladding layer. This measurement was done using *Filmetrics Resist and Dielectric Thickness Mapping System* at the NanoFab facility at the University of Alberta.

dicing tool is 42-54 μm thick and has an RPM of 30000 with a 10-20 mm/sec feed.

A-1.11 Polishing

After obtaining the MZI chips from the dicing step, the inout and output ends were polished before performing experiments in order to reduce light scattering from rough edges. Polishing films with grain size ranging from 15 μm to 0.1 μm were used. Six recipes were developed and tested, as illustrated in Table A-1. Recipe no. 6 produced the most uniform polish (refer Fig. A-6) and hence was selected as the standard polishing recipe for the MZI chips.

Table A-1: Different configurations of the fabricated MZI chips

Recipe 1		**Recipe 2**		**Recipe 3**		**Recipe 4**		**Recipe 5**		**Recipe 6**	
Grain size (μm)	Time (secs)	Grain size (μm)	Time (secs)	Grain size (μm)	Time (secs)	Grain size (μm)	Time (secs)	Grain size (μm)	Time (secs)	Grain size (μm)	Time (secs)
15	50	15	40	15	50	15	10	15	-	15	-
6	15	6	20	6	20	6	20	6	-	6	40
3	15	3	15	3	15	3	-	3	45	3	15
1	15	1	15	1	-	1	-	1	15	1	15
0.5	15	0.5	-	0.5	-	0.5	-	0.5	10	0.5	15
0.1	-	0.1	-	0.1	-	0.1	-	0.1	10	0.1	20

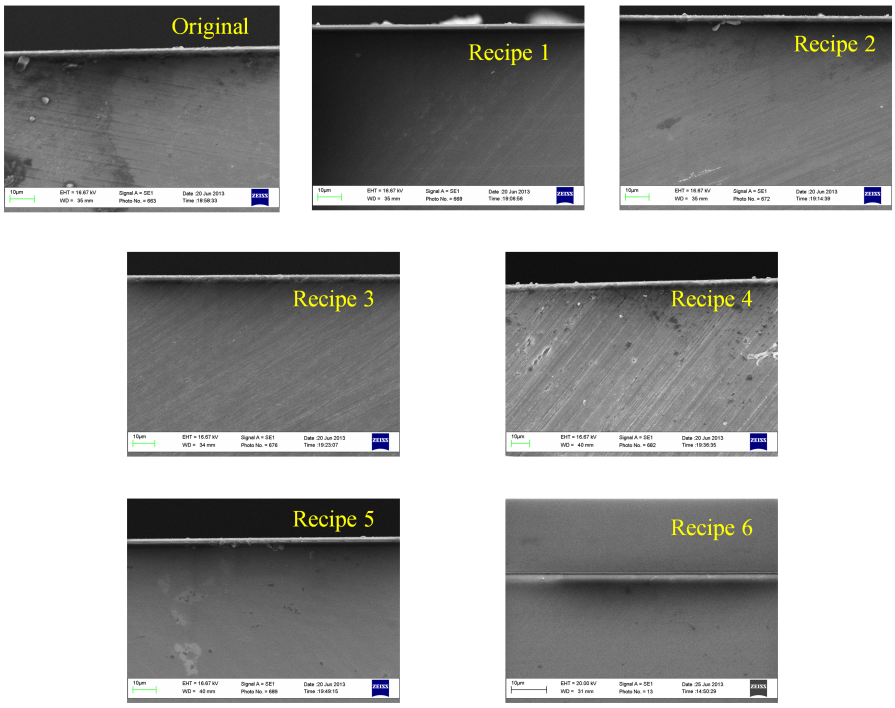

Figure A-6: SEM images of the MZI chip input/output edges with different polishing recipes.

A-2 Error Analysis

We report here the error analysis associated with the experimental calculations performed in Chapter 3.

A-2.1 Error analysis of power measurements

Power measurements at the input and output ends of the MZI biosensor chips were repeated three times for every concentration of the analytes used. Each reading was taken after the power reading in the photodiode was stable for over 5 secs. The MZI biosensors used in these experiments are highly sensitive and hence, there was a small percentage of error, most likely, due to slight changes in temperature or humidity in the laboratory. This error has been manifested in Figs. 3.8 and 3.9 of Chapter 3. Our experiments involved the study of MZI chips with three different microbial solutions: *Listeria monocytogenes*; *E. coli*; and a mixture of *Listeria monocytogenes* and *E. coli*. Table A-2 and A-3 lists the error estimates of each of the microbial solutions in terms of the standard deviation and the % error associated with it. The standard deviation and % error are given by:

$$\sigma = \sqrt{\frac{\sum(x-\bar{x})^2}{N-1}} \qquad (\text{A-1})$$

$$\%error = \frac{\sigma}{\bar{x}} \qquad (\text{A-2})$$

where σ is the standard deviation , x is the value of each reading, $\bar{x}$ is the mean of the readings and N is the number of readings taken, which is 3 is our case.

Table A-2: Standard deviation and percentage error in the power measurements of the MZI biosensor with different concentrations of *Listeria monocytogenes* (refer Fig. 3.8 in Chapter 3)

Listeria monocytogenes		
Conc. (cfu/ml)	σ	% error
2.8E13	0.0165	2.32
2.8E12	0.006	0.86
2.8E10	0.0291	4.33
2.8E9	0.0136	3.40
2.8E8	0.0059	2.31
2.8E7	0.0148	6.66
2.8E5	0.0097	4.95
2.8E4	0.0031	1.71
2.8E3	0.0076	4.31

Table A-3: Standard deviation and percentage error in the power measurements of the MZI biosensor with different concentrations of *E.coli*; and *Listeria monocytogenes* and *E. coli* mixture (refer Fig. 3.9 in Chapter 3)

	***E.coli* only**		***L. monocytogenes* and *E. coli mixture***	
Conc. (cfu/ml)	σ	% error	σ	% error
2.8E9	0.001	0.57	0.0127	4.13
2.8E8	0.0083	4.66	0.0083	3.55
2.8E7	0.0023	1.27	0.01	4.89
2.8E6	0.0047	2.60	0.0104	5.35
2.8E5	0.0062	3.47	0.0014	0.74